Late Paleozoic tectonic history of the Ertix Fault in the Chinese Altai and its implications for the development of the Central Asian Orogenic System

Stephanie M. Briggs†
Department of Earth and Space Sciences, University of California, Los Angeles, California 90095, USA

An Yin‡
Department of Earth and Space Sciences and *Institute of Geophysics and Planetary Physics, University of California, Los Angeles, California 90095, USA*

Craig E. Manning
Department of Earth and Space Sciences, University of California, Los Angeles, California 90095, USA

Zheng-Le Chen
Xiao-Feng Wang
Institute of Geomechanics, Chinese Academy of Geological Sciences, Beijing 100081, People's Republic of China

Marty Grove
Department of Earth and Space Sciences, University of California, Los Angeles, California 90095, USA

ABSTRACT

The Central Asian Orogenic System (CAOS) is one of the largest Phanerozoic accretionary orogens in the world and may represent a significant site of continental growth. Its origin has been explained by two competing models: syn-subduction strike-slip duplication of a single (>1000 km) long-lived arc (ca. 630–360 Ma) or collision of multiple arcs and micro-continents. Central to the debate are the relative roles of syn-subduction strike-slip faulting versus thrusting. In both models, the Ertix fault figures prominently, either as a roof fault of a large strike-slip duplex system developed during oceanic subduction or as a suture of arc-continent or continent-continent collision. In order to differentiate between the above models, we conducted field mapping, detailed kinematic analysis, and geochronological dating of the Ertix fault zone in the Chinese Altai. Our work indicates that the fault is a crustal-scale thrust that was active in the Permian. Its hanging wall records two pulses of magmatism ca. 450 Ma and ca. 280 Ma and experienced peak pressure and temperature of 6.2–7.7 kbar and 560–670 °C. Our geologic observations, together with the existing geologic information, favor a tectonic model that involves two episodes of subduction below the Altai arc: first, in the Ordovician, along a south-dipping subduction zone; and second, in the late Carboniferous and early Permian along north-dipping subduction of the Junggar ocean. It was during the latter event that a mélange complex was underplated below the older Ordovician arc, metamorphosed at lower crustal depths, and then exhumed to the upper crust along the south-directed Ertix thrust zone.

Keywords: Ertix, Irtysh, central Asia, magmatism, Xinjiang, deformation

INTRODUCTION

The 8000-km by 6000-km Central Asian Orogenic System (CAOS), also referred to as the Central Asian Fold Belt, Ural-Mongol Fold Belt, or the Altaids, is located between the European, Siberian, North China, and Tarim cratons and is responsible for a greater volume of new crust in the Phanerozoic than the Mesozoic North American Cordillera (Fig. 1; Zonenshain et al., 1990; Şengör et al., 1993; Jahn, 2004) (Fig. 1 is also available in color as Fig. DR1; see footnote 1). Due to the lack of modern geologic studies, the mechanism by which the mountain belt was constructed remains poorly understood (Badarch et al., 2002; Windley et al., 2002). The origin of the CAOS has been explained by two competing models: syn-subduction strike-slip duplication of a single (>1000 km), long-lived (630–360 Ma) arc (e.g., Şengör and Natal'in, 1996), or collision of multiple island arcs, oceanic complexes, and continental blocks (e.g., Zonenshain et al., 1990; Dobretsov et al., 1995; Badarch et al., 2002). Central to the debate on the growth mechanism of the CAOS is the relative role of syn-subduction strike-slip faulting and thrust-related deformation. In both models, the Ertix fault (alternatively transliterated as the Irtysh, Erqis, or Erqishi fault; Şengör and Natal'in, 1996; Windley et al., 2002; Laurent-Charvet et al., 2002) is a key structure. It is interpreted as either a strike-slip fault accommodating >1000 km of right-slip motion (Şengör and Natal'in, 1996) or a suture between the Altai arc to the north and the Junggar microcontinental block to the south (Coleman, 1989; Zonenshain et al., 1990; Dobretsov et al., 1995; Badarch et al., 2002). This fault is traceable for >1000 km from Kazakhstan to NW China and may have extended farther to the southwest part of Mongolia for an additional 1500 km, making its total

†E-mail: sbriggs@ess.ucla.edu.
‡Also at School of Earth Sciences and Resources, China University of Geoscience, Beijing 100083, China

GSA Bulletin; July/August 2007; v. 119; no. 7/8; p. 944–960; doi: 10.1130/B26044.1; 11 figures; 4 tables; Data Repository item 2007146.

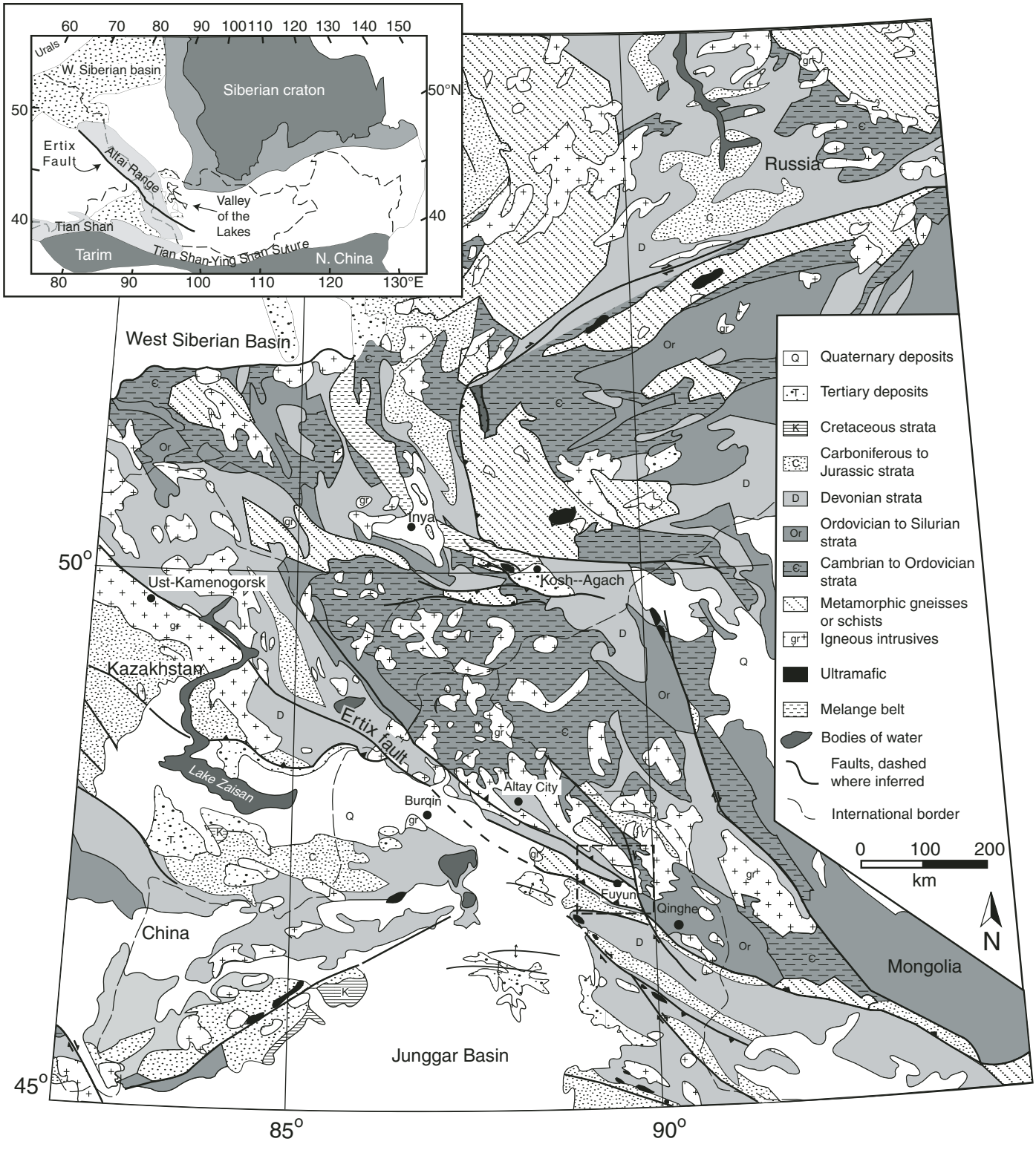

Figure 1. Regional geologic map of the Altai Mountains and its neighboring regions, adapted from Li (1997). Location of Figure 2 is shown with dashed box. Inset is geographic map of central Asia.

length >2500 km (Şengör et al., 1993; Şengör and Natal'in, 1996; Cunningham et al., 1996; Badarch et al., 2002) (Fig. 1). Because of its central position in the overall architecture of the CAOS, determining the kinematic history of the Ertix fault is vital to understanding the evolution of this vast accretionary orogen.

We studied the Ertix fault where it is exposed in NW China, near the southern edge of the Chinese Altai Mountains. The Altai Mountain range is ~2500 km long, stretching across Russia, Kazakhstan, western China, and western Mongolia, and occupying the south-central part of the CAOS (Figs. 1 and 2). (Note: Color versions of Figures 1, 3, and 5 are available in the GSA Data Repository[1].) The Cenozoic Junggar basin bounds the Altai Range to the south, whereas the Valleys-of-Lakes in western Mongolia is its northern boundary (Badarch et al., 2002). The results of our combined kinematic, metamorphic, geochronologic, and thermochronologic studies presented below reveal that in NW China, the Ertix fault is a thrust that exhumed upper amphibolite facies gneisses and Early Paleozoic granitoids from middle crustal depths to shallow crustal levels in the Permian ca. 290–260 Ma, during a prominent regional contractional event.

GEOLOGIC BACKGROUND

The Alpine orogenic belt of Eurasia is the site of continental growth in the Mesozoic and Cenozoic, whereas the development of the CAOS is primarily responsible for the growth of the Eurasian continent in the Paleozoic (e.g., Şengör et al., 1993; Şengör and Natal'in, 1996; Yin and Harrison, 2000). The CAOS is composed of continental blocks, accretionary complexes, and arcs that were accreted onto the Siberian craton to the north. The southern boundary of these accreted terranes is the Tian Shan-Ying Shan suture system along the north edge of the Tarim-North China craton (Fig. 1; Zonenshain et al., 1990; Allen et al., 1993; Yin and Nie, 1996; Şengör and Natal'in, 1996). Based on an interpretation that the amalgamation of the CAOS was completed by the Carboniferous to Early Permian (Coleman, 1989; Zonenshain et al., 1990; Allen et al., 1992 Allen et al., 1993, Lyons et al., 2002), numerous Late Permian plutons in the region are interpreted as "post-collisional" or "anorogenic" granites (Coleman, 1989; Wickham et al., 1996; Chen and Jahn, 2002, 2004; Liu and Fei, 2006). With the exception of latest Paleozoic to Mesozoic strike-slip faults in Mongolia and Russia (e.g., Lamb et al., 1999; Buslov et al., 2004), the Mesozoic is generally considered a period of relative tectonic quiescence that was followed by renewed uplift and deformation over the Altai region due to the Indo-Asian collision in the Cenozoic (e.g., Bullen et al., 2001; Delvaux et al., 1998; Cunningham et al., 1996, 1996). However, some have argued (e.g., Hendrix et al., 1996; Webb and Johnson, 2005) that the southernmost part of the CAOS in Mongolia experienced significant Mesozoic shortening and extension.

Previous Work

The Ertix fault is covered by Quaternary sediments of the Western Siberian Basin, thus how the fault terminates in the north is not clear (Fig. 1). In Kazakhstan, the Ertix shear zone consists of a >10 km-thick shear zone that strikes N45°W and dips 50–80°NE. (Mileyev et al., 1980; Rotarash et al., 1982). High-grade rocks in the shear zone are mylonitic granitoids, blastomylonite, and amphibolite (Mileyev et al., 1980; Chikov et al., 1988; Travin et al., 2001; Buslov et al., 2004). The shear zone also consists of mélange and ophiolitic rocks (Mileyev et al., 1980; Rotarash et al., 1982; Buslov et al., 2004). Northeast of the shear zone and the associated high-grade rocks are Devonian to Carboniferous shale, siltstone, and calcareous sandstone, whereas southeast of the shear zone a middle Devonian to lower Carboniferous island arc complex is exposed (Rotarash et al., 1982; Zonenshain et al., 1990; Vladimirov et al., 1997; Mitrokhin et al., 1997). The Devonian-Carboniferous rocks mentioned above all have experienced greenschist facies metamorphism and were subsequently intruded by the Permian Kalba-Narym and Kalbinsky batholiths (Mileyev et al., 1980; Zonenshain et al., 1990; Travin et al., 2001).

In China, the Ertix fault is locally covered by Quaternary sediments along the northeastern edge of the Junggar basin (Fig. 1). The fault is well exposed near the town of Fuyun in the southwestern Chinese Altai, where it separates the high-grade Ertix gneiss complex (also sometimes referred to as the Kalaerqis gneiss complex) to the north from Devonian to Carboniferous volcanic and clastic deposits to the south (Fig. 2; Xinjiang BGMR, 1978, 1993). The Ertix gneiss complex, composed of schist and gneiss, is variably interpreted as Precambrian basement (He et al., 1990; Qu and Chong, 1991; Zhang et al., 2005), a Paleozoic accretionary wedge (O'Hara et al., 1997), or a 10-km-thick mylonitic shear zone (Windley et al., 2002). The fault is consistently mapped as a north-dipping structure with an average strike of N40°W, though the strike of the fault changes locally to N70°W in our field area. In the eastern portion of the study area, the Ertix fault is truncated and offset ~10–20 km by the well-known, active, N-striking right-slip Fuyun fault, which was responsible for the 1931 M_W 8 Fuyun earthquake (Fig. 2; Xinjiang BGMR, 1978; Tapponnier and Molnar, 1979).

Farther to the east, the trace of the Ertix fault in Mongolia is uncertain due to the lack of detailed geologic studies across the China-Mongolia border. Cunningham et al. (1996) correlated the Ertix fault from China with the Bulgan oblique thrust fault, which places high-grade gneisses and schists against granite, greenschist, and quartzite in western Mongolia. In the existing regional syntheses of Mongolian geology, the Ertix fault is correlated with a suture zone marked by an east-trending ophiolite belt in south-central Mongolia (e.g., Badarch et al., 2002). This belt is interpreted by Xiao et al. (2004) as the locus of a backarc basin that was closed by collision between a Devonian arc along the Mongolian-China border to the south and the Siberian craton and its fringing arcs to the north.

The kinematics of the Ertix fault are variably interpreted in the competing tectonic hypotheses about the evolution of the CAOS. In the syn-subduction strike-slip duplex model, the Ertix fault is a major strike-slip roof fault in a large duplex system that had accommodated ~1000 km right-slip motion from the Ordovician to Early Permian (ca. 500–300 Ma) (Şengör and Natal'in, 1996). Building upon this work, Allen et al. (1995) interpret the Ertix fault to have reversed its shear sense from right-slip motion during mid- to late Paleozoic oceanic subduction to left-slip motion in the Late Permian and Triassic during intra-continental deformation. This change in the sense of slip on the Ertix fault and its synchronicity with northwest-striking left-slip faulting in the Tian Shan some 500–800 km to the south was proposed to cause the opening of the Junggar basin as a large intracontinental pull-apart basin between the two left-slip faults (Allen et al., 1995). In contrast to the emphasis on a strike-slip history for the Ertix fault, several workers interpret the Ertix fault to be a major late Paleozoic thrust (He et al., 1990; Qu and Zhang, 1994) or even a suture (Coleman, 1989; Zonenshain et al., 1990; Dobretsov et al., 1995; Badarch et al., 2002). These models suggest significant Permian shortening and exhumation during motion on the Ertix fault after ocean closure.

Geologic studies along the Ertix fault zone so far appear to support both strike-slip and thrust faulting models. In Kazakhstan, Vladimirov

[1]GSA Data Repository item 2007146, color versions of selected figures, electron probe analyses, complete U-Pb and Ar/Ar isotopic data tables and zircon cathode-luminescence images, is available on the Web at http://www.geosociety.org/pubs/ft2007.htm. Requests may also be sent to editing@geosociety.org.

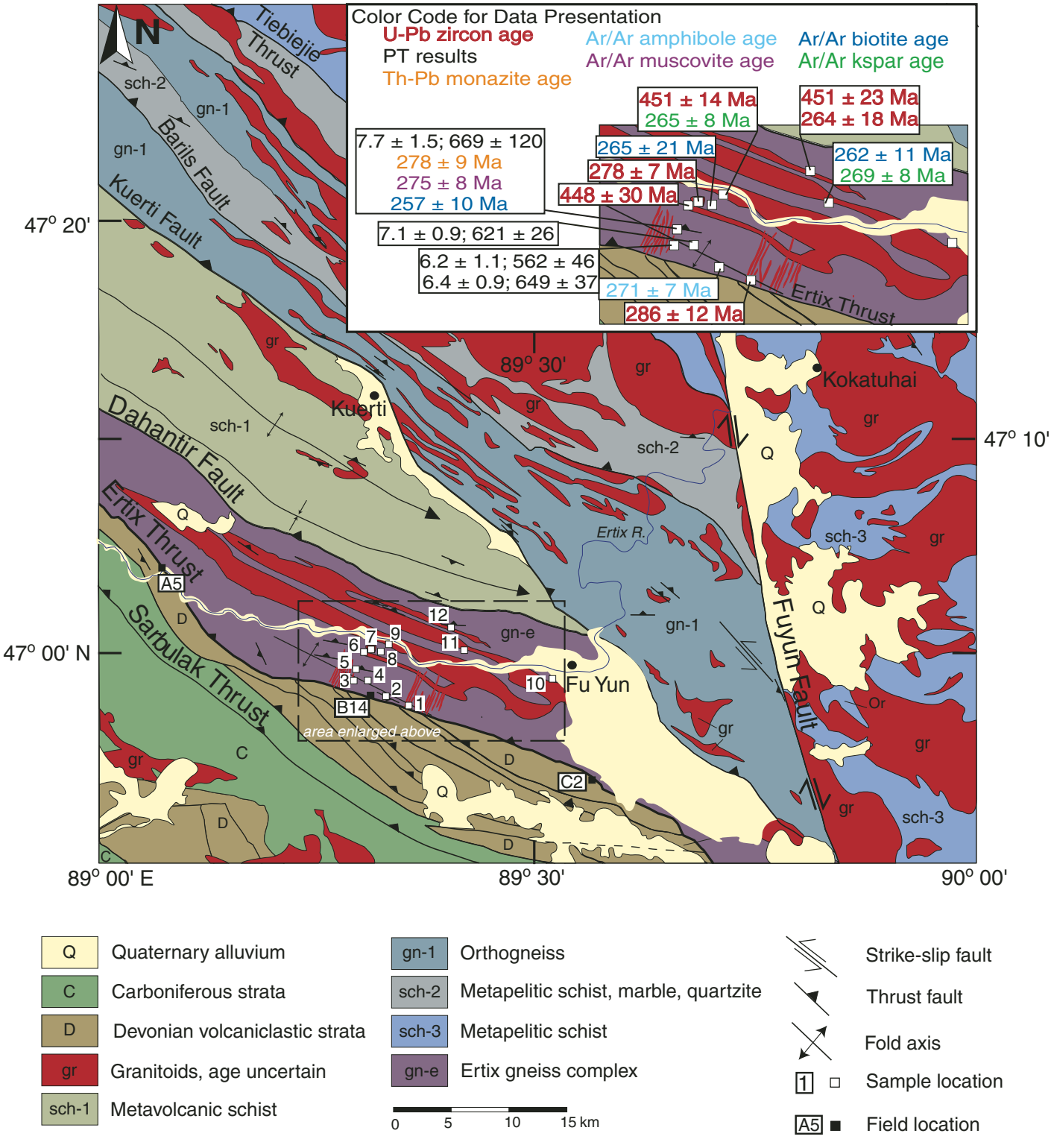

Figure 2. Geologic map of area near Fuyun, Chinese Altai, in western China, adapted from Xinjiang BGMR, 1978. Dashed box shows area of inset, which is an enlargement showing analytical samples and results summary. Key field locations discussed in text are marked by black squares; analytical sample locations are marked with white squares and sample location number.

et al. (1997) report only left-slip deformation, while Mitrokhin et al. (1997) report conflicting left-slip and right-slip shear indicators from the Ertix fault zone. In contrast, Mileyev et al. (1980) found steeply NE-plunging down-dip mineral stretching lineation in the shear zone as evidence for thrusting. Similar conflicting fault kinematics are also reported on the Ertix fault in the Chinese Altai. For example, Qu and Zhang (1994) document mainly thrust kinematics on the Ertix fault, while more complicated strike-slip and thrust kinematics are reported by Laurent-Charvet et al. (2003). These studies have neglected to correlate local fault strike with striation directions. For example, a thrust salient with lateral ramps at its two ends would generate strike-slip kinematics: one is right-slip and the other left-slip. As shown in our study, this may be the case for the Ertix fault.

Because of its central importance in tectonic models for the region, geochronological studies of the Ertix fault deformation have been attempted. In Kazakhstan, $^{40}Ar/^{39}Ar$ mica, amphibole and K-feldspar cooling ages of 263–283 Ma are used to date the timing of left-slip fault motion (Vladimirov et al., 1997; Travin et al., 2001). In China, Laurent-Charvet et al. (2003) report $^{40}Ar/^{39}Ar$ biotite and amphibole ages between 244 and 265 Ma on amphibolite-grade gneisses north of the Ertix fault. Qu and Zhang (1994) cite a Permian age for a conglomerate unit unconformably overlying the Ertix fault and therefore interpret fault motion to be older than ca. 280 Ma. Often, timing of strike-slip motion is interpreted as synchronous with cooling indicated by $^{40}Ar/^{39}Ar$ thermochronometry, though no structural mechanisms for how strike-slip motion could produce such cooling, such as shear heating or exhumation by oblique slip, have been proposed (e.g., Vladimirov et al., 1997; Travin et al., 2001).

Geology of the Fuyun Area

The northwest-trending Chinese Altai parallels the strike of major faults along its southern margin, including the Ertix fault. This structural configuration is well expressed in the Fuyun area where we conducted our field research. In the study area, six major northeast-dipping faults are exposed (Fig. 2). From south to north, they are the Sarbulak thrust, Ertix fault, Dahantir fault, Kuerti thrust, Barils thrust, and Terbiejie thrust system. In the southernmost part of the study area, the Sarbulak footwall is composed of Carboniferous volcaniclastic strata. Its hanging wall consists of Carboniferous and Devonian volcaniclastic strata that are duplicated by a thrust duplex system (Fig. 2). To the north, the Ertix fault juxtaposes the low-grade Carboniferous to Devonian volcaniclastics in the footwall and the high-grade Ertix gneiss complex in the hanging wall (gn-e, Fig. 2). The Ertix gneiss complex is a heterogeneous package of foliated amphibolite-grade metapelite, para- and orthogneisses, metabasite, and metachert; their protolith ages are estimated from Proterozoic (Qu and Zhang, 1994) to Carboniferous (Xinjiang BGMR, 1978). Deformed granitic intrusions demonstrate the same foliation seen in the gneiss complex, though limited exposures of undeformed granitoids (small plutons and dikes) that cross-cut regional foliation also exist. The northern boundary of the Ertix gneiss complex is the Dahantir fault, which was interpreted by Qu and Zhang (1994) as a thrust. North of the Dahantir fault, meta-volcanic and meta-sedimentary rocks have been broadly folded (~10 km wavelength) into an east-plunging anticline-syncline pair that is truncated to the north and east by the range-bounding Kuerti fault (Fig. 2). The hanging wall of the Kuerti fault is an exposed orthogneiss unit (gn-1 in Fig. 2), which is the footwall to the Barils thrust farther north. North of the Barils thrust are metapelite schists, marble, and quartzite (Xinjiang BGMR, 1978; Qu and Zhang, 1994). The northern boundary of the metamorphic sequence is the Terbiejie thrust system, which exposes a metasedimentary sequence assigned to be Cambrian-Ordovician in age by Xinjiang BGMR (1978) to the north. The map area is intruded extensively by variably deformed granitoids. They are typically assigned "Caledonian" (early Paleozoic) and "Hercynian" (late Paleozoic) ages (Chen and Jahn, 2002). These granitoids and all the Paleozoic units are cut by the active Fuyun fault.

METHODS

In order to elucidate the tectonic history of the Ertix fault, we conducted geologic mapping in the Fuyun area in the southwestern Chinese Altai (Fig. 2). Our mapping was built upon an existing Chinese geologic map at a scale of 1:200,000 (Xinjiang BGMR, 1978). The map provides useful information on distribution of major lithologic units and biostratigraphic controls on the ages of sedimentary units. However, it lacks critical information on fault kinematics, metamorphic conditions, and radiometric ages of metamorphic and igneous rocks. To overcome these problems, our field investigation focused on fault geometry and kinematics, field relationships between structures and distribution of metamorphic grades across the Ertix fault zone, and collection of key geochronological samples that elucidate the ages of metamorphism and igneous activity.

In order to determine metamorphic conditions of high-grade rocks in our study area, we conducted thermobarometric studies in the Ertix hanging wall. The UCLA JEOL JXA-8200 electron microprobe was used to make X-ray composition maps of garnets to assess zoning patterns, as well as to measure mineral compositions. An accelerating voltage of 15 kV and a current of ~100 nA were used for X-ray maps collected with 2 μm pixels with a dwell time of 60 msec per pixel. For individual mineral analyses, a current of 10 nA was used with a beam focused to <1 μm diameter for all phases but plagioclase and micas, which required a diameter of 4–7 μm. We measured coexisting phases (e.g., garnet, amphibole and plagioclase) in 4–8 regions within each sample, and then used the programs A-X and THERMOCALC (Holland and Powell, 1998) to calculate pressure-temperature (*P-T*) intersections of all equilibria. For each sample, we then calculated the weighted mean of the *P* and *T* determinations for the different regions with uncertainty given at the 2σ confidence level.

The age of metamorphism and its relationship to deformation were investigated using in situ Th-Pb dating of monazite. This method allows direct examination of the textural relationships between monazite grains and metamorphic or tectonic fabrics (Harrison et al., 1995). Monazite, often very small (<15 μm in diameter), appears bright when using the scanning electron microscope (SEM) in backscatter mode. Once identified, we used the ion microprobe to date grains in situ following procedures in Catlos et al. (2002). The UCLA CAMECA IMS-1270 secondary ion microprobe was used with a beam current of 10–15 nA focused to a size of 15–30 μm in diameter. Monazite standard 554 (45 ± 1 Ma; Harrison et al., 1995) was used and checked against a second standard, 83-32 (2685 ± 2 Ma; Corfu, 1988) with U and Th compositions more similar to the unknowns.

For U-Pb geochronology, zircons were separated, mounted in epoxy, and polished along with grains from zircon standard AS3, then analyzed with the UCLA CAMECA IMS-1270 secondary ion microprobe following procedures reported by Quidelleur et al. (1997). A 15 nA O^- primary beam current was focused to a spot of 30–40 μm diameter. To improve secondary ionization of Pb^+, the sample surface was flooded with O^{-2} at a pressure of ~3×10^{-5} torr (1 torr = 133.322 Pa). Weighted mean ages of the zircon standard AS3 yielded a dispersion of <1% from the age given by thermal ionization mass spectrometry (Paces and Miller, 1993). Grains were inspected with a cathode luminescence (CL) detector on a scanning electron microscope to aid in age interpretation.

For $^{40}Ar/^{39}Ar$ analysis, concentrates of amphibole, biotite, muscovite, and K-feldspar were separated and hand-picked. Mineral separates of unknown age and sanidine from the 27.8 Ma Fish Canyon Tuff (Cebula et al., 1986; Renne et al., 1994) were irradiated for 15–45 h at the University of Michigan and McMaster University. Roughly 4–15 mg of material was step-heated in a double vacuum furnace, and isotopic compositions of the released gas were measured using a VG 1200 automated mass-spectrometer at UCLA. Data were reduced using the in-house data-reduction program AGECAL.EXE, and uncertainties were calculated to the 95% confidence level. However, the final results do not include uncertainties in the J-factors or decay constants.

NEW STRUCTURAL GEOLOGY

South and west of Fuyun, the Ertix fault is best exposed as a 2–15-cm-thick gouge zone (Fig. 3A; also available in color as Fig. DR2, see footnote 1). At some locations the fault is also associated with mylonitic shear zones directly above the brittle fault zone. Based on outcrop patterns, the fault trace can be located within a few meters in areas of poor exposure by the abrupt change in lithology and metamorphic grade.

In map view, the Ertix fault strikes ~N40°W with a local N70°W jog in the central portion of the mapped area (Fig. 2). South of the Ertix fault, imbricate thrusts repeat Devonian strata and carry them over Carboniferous rocks (Fig. 2). Spaced cleavage is well developed in the units south of the Ertix fault and dips steeply to the NE or SW. North of the Ertix fault, foliation within the Ertix gneiss complex dips 40–80° to the northeast, with the exception of the southwesternmost portion of the complex in the map area, where foliation dips steeply to the southwest (55–85°; Fig. 2). Fold axes are aligned parallel to the regional trace of the fault and plunge shallowly to the east and southeast (Fig. 3C). The hanging-wall is intruded by undeformed granitoids and a series of NNE-striking granitic dikes that are 1–3 km long and <10 m thick. These vertical dikes are generally orthogonal to the local strike of the Ertix fault, and their tectonic origin is unclear. In the center of the Ertix hanging wall, ~3–5 km north of the fault, a large (>1 km wide across strike) exposure of K-feldspar + quartz + hornblende + plagioclase + biotite orthogneiss is found along the Ertix river.

Generally, brittle deformation features such as striations and gouge zones are exposed within <50 m of the fault, but evidence of ductile folding associated with fault motion is observed up to 1.5 km north of the fault. Within 100 m of the fault trace there are moderate to steep

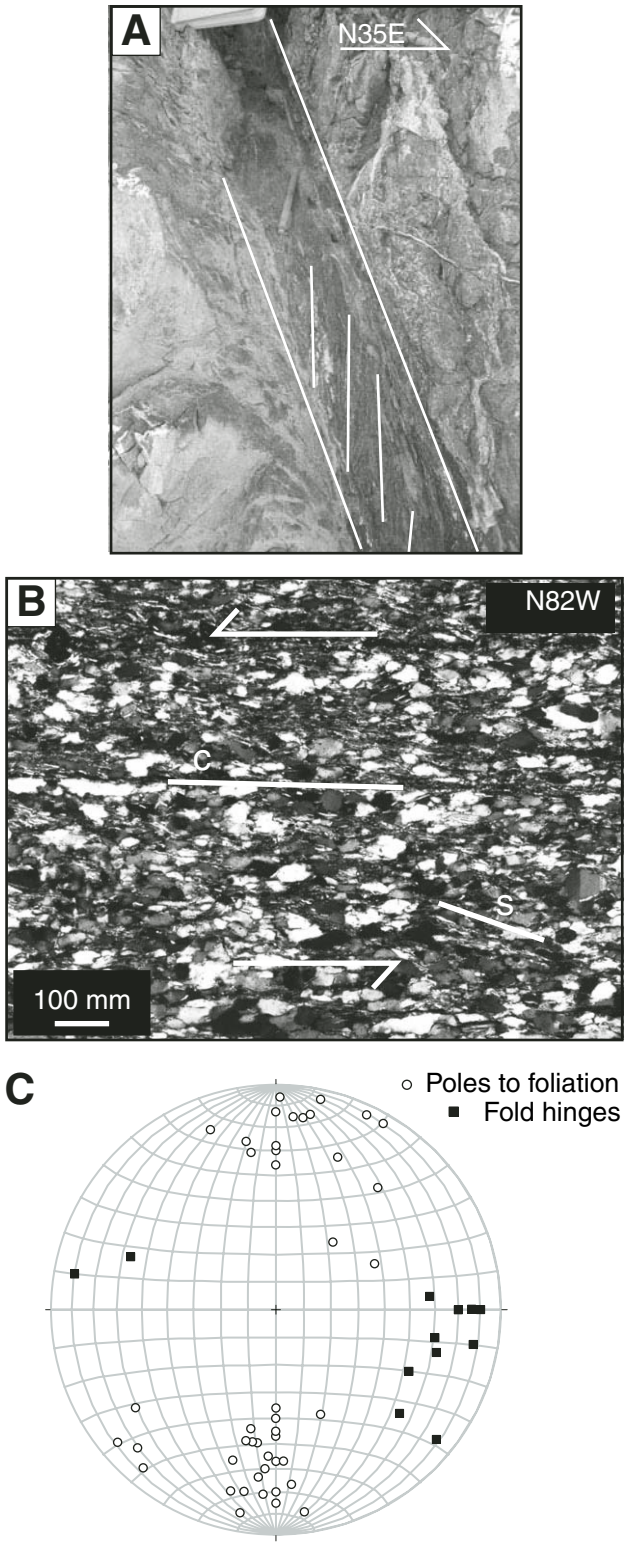

Figure 3. Field photos and structural data. (A) Photo looking W-NW at gouge zone with steeply N-dipping cleavage, consistent with thrusting at location A5 (Fig. 2). (B) Photo-micrograph of mylonite at location B14 (Fig. 2) and labeled S-C fabrics indicating left-slip collected along N70W striking fault segment C. Lower hemisphere projection of fold hinges and poles to foliation throughout Ertix hanging wall. Foliation is dominantly NE-dipping; subhorizontal fold hinges plunge gently to the southeast, consistent with south-directed contraction.

northeast-dipping fault gouge zones with well-developed fault-zone cleavage oblique to the bounding fault surface. Their relationship indicates top-south thrust transport (at two locations, A5 and C2; Figs. 2, 3A). At location A5, we observe a lone down-dip striation plunging 65° to N20°W on a fault oriented N35°W 72°NE. Between these two locations, outcrops of phyllite (location B14) exhibit a gently plunging mineral stretching lineation trending parallel to local strike of the fault. Foliation is defined by alignment of micaceous minerals, whereas the lineation present at location B14 is defined by elongation and rodding of quartz grains. S-C fabrics defined by the micaceous minerals in oriented thin sections (cut perpendicular to foliation and parallel to lineation) indicate left-slip motion on the N70°W-striking segment of the Ertix fault (Fig. 3B). The Ertix fault segments, which exhibit thrust-sense indicators, strike N35°W, whereas the segment exhibiting left-slip indicators is oriented N72°W. This observation suggests a common transport direction, but the fault's kinematics depend on its local orientation. Since the portions of the fault that strike NW have the same orientation as the regional fault strike, they are taken as more representative of the overall sense of shear and style of deformation for the Ertix fault and indicate that it is a SW-directed thrust. That is, the lineation at location A5 indicates a ~S40°W transport direction for the Ertix fault, and strike-slip indicators on the central N75°W striking segment are the result of an oblique-ramp caused by a bend in fault strike.

ANALYTICAL RESULTS

Here we present results of our analytical studies aimed at understanding the metamorphic, intrusive, and cooling history of rocks in the Ertix hanging wall. Results are organized by technique, and by sample numbers, which increase with distance from the fault. Sample numbers followed by a letter represent different samples collected at the same outcrop or field location. Unless otherwise stated, errors are 2σ.

Thermobarometry

Representative mineral compositions are listed in Table 1, and all calculated *P-T* conditions are listed in Table 2; the average *P-T* conditions for each sample is shown as an error ellipse in Figure 4. The complete set of mineral analyses can be accessed as GSA Data Repository Table DR1 (see footnote 1).

The hanging wall adjacent to the fault is dominated by garnet-amphibolite schist. A garnet-hornblende-plagioclase (An_{42}) schist from 150 m north of the fault (field location 3a, Fig. 2) contains garnet that is unzoned, except for a minor increase in Mn found at the outermost 10 μm rim of 1–3 mol%. We avoided the high-Mn rim while collecting analyses of coexisting minerals, making use of inclusions in garnet when possible. Using the garnet-hornblende-plagioclase-quartz thermobarometry of Dale et al. (2000), we obtain a temperature of 560 ± 50 °C and a pressure of 6.2 ± 0.9 kbar (Fig. 4). A second sample (3b) of the garnet amphibolite was also collected at the same location. Plagioclase (An_{31}) and hornblende are unzoned, while garnets display prograde growth zoning, with no obvious chemical evidence for resorption (e.g., no Mn-rich rim). Seven sets of analyses for this schist have compositions that correspond to a metamorphic temperature of 650 ± 40 °C and a pressure of 6.4 ± 1.0 kbar (Fig. 4).

Three hundred and fifty meters north of the Ertix fault, a pelitic schist at location 4 (Fig. 2) has garnet, biotite, muscovite, and plagioclase (An_{37}). Garnets display Mn-rich rims (≤10 μm wide) indicative of retrogression, but are otherwise homogeneous. Using analyses from the core of garnets, quantitative thermobarometry on the schist yielded similar temperature conditions and a slightly higher metamorphic pressure than those found at location 3 (620 ± 30 °C, 7.1 ± 0.9 kbar; Fig. 4).

Sample 5c bears the assemblage of garnet-biotite-plagioclase-K-feldspar-quartz-rutile-ilmenite, and inclusion trail patterns in many garnets suggest synkinematic growth. Garnets are zoned, with Mn, Ca, and Fe/Fe+Mg concentrations highest in garnet cores and decreasing toward the rim (Fig. 5A, also available in color as Fig. DR3, see footnote 1). The outermost <25 μm of the garnet displays increased Mn and Fe/Fe+Mg. This compositional variation is consistent with zoning expected if the garnet initially grew during prograde metamorphic conditions but was later modified by retrogression. Plagioclase inclusions in garnets are most Ca-rich ($X_{an} \leq 90$) near the garnet core and most sodic when trapped near the rim (X_{an} ~30). Investigations into the possibility of retrograde net transfer reactions have found that this sample may have experienced ~1% dissolution following methods in Kohn and Spear (2000). Correcting biotite and garnet compositions typically yielded *P-T* conditions slightly (<20 °C) lower than conditions calculated from raw compositions. The intersections of garnet-biotite and garnet-rutile-ilmenite-plagioclase-silica equilibria (GRIPS) yield *P-T* conditions of 670 ± 120 °C and 7.7 ± 1.5 kbar for this sample (Tables 1 and 2, Fig. 4).

TABLE 1. REPRESENTATIVE ANALYSES FOR THERMOBAROMETRY RESULTS

	3a			3b			4				5c				
	Grt	Hbl	Pl	Grt	Hbl	Pl	Bt	Grt	Ms	Pl	Bt	Grt	Pl	Kfs	Ilm
TiO_2	0.08	0.51	0.03	0.05	0.59	0.04	1.61	0.04	0.54	0.01	2.36	0.12	0.00	0.08	55.40
SiO_2	37.47	42.73	58.27	37.45	44.07	60.43	42.33	37.20	47.70	58.03	34.81	37.59	59.55	63.47	0.04
Na_2O	0.02	1.27	6.53	0.02	1.66	8.00	0.22	0.01	0.91	7.06	0.17	0.00	8.33	0.41	0.02
FeO	21.43	18.08	0.03	28.64	18.42	0.43	13.54	27.12	1.22	0.15	19.42	30.32	0.18	0.33	41.79
K_2O	0.00	0.57	0.05	0.00	0.42	0.08	8.93	0.01	9.84	0.06	9.52	0.00	0.13	15.96	0.03
Cr_2O_3	0.01	0.00	0.00	0.00	0.00	0.00	0.00	0.00	0.00	0.00	0.00	0.00	0.00	0.00	0.00
Al_2O_3	21.38	14.51	27.74	21.51	14.32	24.63	18.18	21.28	35.56	25.86	20.45	21.86	24.78	18.45	0.02
MgO	2.50	8.74	0.00	3.24	9.19	0.01	11.66	3.11	0.57	0.00	9.05	3.22	0.01	0.00	0.05
MnO	10.64	0.76	0.00	5.42	0.46	0.00	0.28	8.41	0.00	0.04	0.33	5.12	0.00	0.03	4.60
CaO	6.64	11.24	9.00	4.84	10.53	6.01	0.03	3.35	0.00	7.69	0.02	3.25	6.21	0.15	0.11
Total	100.17	98.40	101.65	101.17	99.66	99.62	96.79	100.53	96.33	98.90	96.13	101.49	99.18	98.86	102.05
	P	T	Cor	P	T	Cor		P	T	Cor			P	T	Cor
Calculated P-T	6.1 (1.1)	592 (50)	0.61	6.4 (1.3)	653 (52)	0.63		7.2 (1.1)	616 (31)	0.80			8.0 (1.9)	662 (146)	0.89

Note: Mineral abbreviations after Kretz, 1983. All Fe as FeO. Uncertainties (in parentheses) are 1σ. Cor—correlation coefficient from THERMOCALC; P—pressure; T—temperature.

TABLE 2. THERMOBAROMETRY RESULTS

Sample	Minerals	P kbar	T °C	Cor
3a	Grt Pl Qtz Hbl	6.4 (1.3)	537 (50)	0.64
3a	Grt Pl Qtz Hbl	6.5 (1)	550 (44)	0.69
3a	Grt Pl Qtz Hbl	5.7 (1.2)	569 (45)	0.63
3a	Grt Pl Qtz Hbl	6.1 (1.1)	592 (50)	0.61
Weighted Average		6.2 ± 1.1	562 ± 46	0.64
3b	Grt Pl Qtz Hbl	6.4 (1.3)	653 (52)	0.63
3b	Grt Pl Qtz Hbl	6.4 (1.3)	653 (52)	0.68
3b	Grt Pl Qtz Hbl	6.3 (1.2)	661 (45)	0.81
3b	Grt Pl Qtz Hbl Kfs	5.8 (2.9)	540 (112)	0.61
3b	Grt Pl Qtz Hbl	6 (1.3)	653 (56)	0.60
3b	Grt Pl Qtz Hbl	7.4 (1.4)	676 (58)	0.63
3b	Grt Pl Qtz Hbl Bt	6.1 (1.2)	640 (43)	0.80
3b	Grt Pl Qtz Hbl	6.2 (1.3)	635 (54)	0.61
Weighted Average		6.4 ± 0.9	649 ± 37	0.67
4	Grt Pl Qtz Bt Ms	7 (1)	612 (29)	0.79
4	Grt Pl Qtz Bt Ms	6.8 (1)	624 (30)	0.79
4	Grt Pl Qtz Bt Ms	7 (1)	612 (29)	0.79
4	Grt Pl Qtz Bt Ms	7.4 (1.2)	636 (34)	0.79
4	Grt Pl Qtz Bt Ms	7.2 (1.1)	616 (31)	0.80
4	Grt Pl Qtz Bt Ms	8.9 (2.7)	690 (83)	0.78
Weighted Average		7.1 ± 0.9	621 ± 26	0.79
5c	Grt Pl Qtz Ru Ilm Kfs Bt	8.9 (2.1)	698 (155)	0.90
5c	Grt Pl Qtz Ru Ilm Kfs Bt	7.7 (1.8)	655 (144)	0.90
5c	Grt Pl Qtz Ru Ilm Kfs Bt	8.0 (1.9)	662 (146)	0.89
5c	Grt Pl Qtz Ru Ilm Bt	7.8 (1.9)	685 (153)	0.88
5c	Grt Pl Qtz Ru Ilm Bt	7.3 (1.7)	631 (137)	0.88
5c	Grt Pl Qtz Ru Ilm Kfs Bt	6.9 (1.8)	700 (159)	0.87
Weighted Average		7.7 ± 1.5	669 ± 120	0.89

Note: Calculations from THERMOCALC v3.1 with May 2001 database (Holland and Powell, 1998). Mineral formulas and activities were calculated with the program A-X by Tim Holland and Roger Powell. Uncertainties are ±1σ for each individual analysis, but weighted averages are listed at the 95% confidence level. "Cor" is correlation coefficient from THERMOCALC; mineral abbreviations after Kretz (1983).

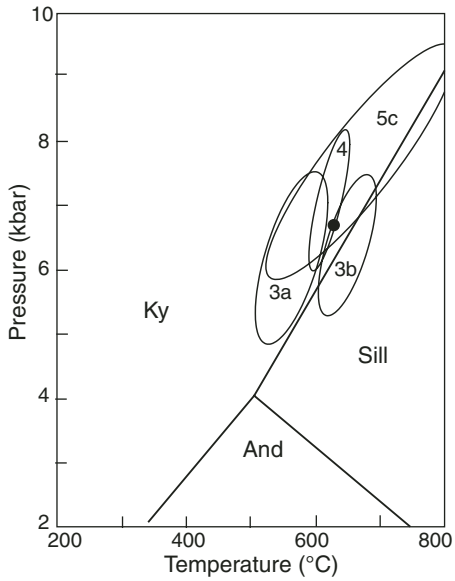

Figure 4. Thermobarometry results, plotted as 2σ error ellipses for each sample. Aluminosilicate triple junction shown for reference; average pressure and temperature from the four samples shown by solid dot. And—andalusite; Ky—kyanite; Sill—sillimanite.

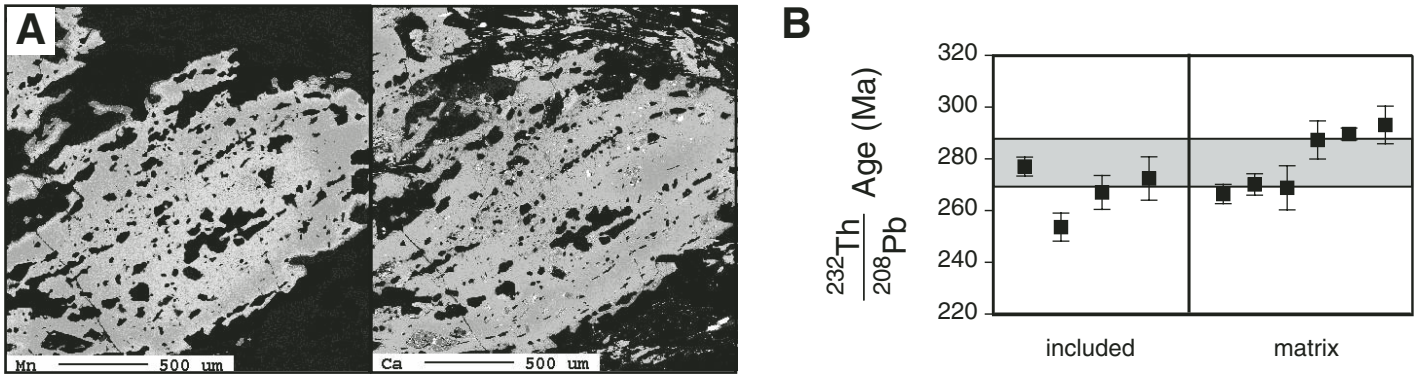

Figure 5. (A) X-ray maps of Mn and Ca concentrations in garnet from sample 5c. Scale bar—500 microns. (B) Th-Pb monazite results from same sample. Grey bar indicates weighted mean of all analyses plus 2σ.

All together, the four samples show some variation in recorded *P-T* conditions but broadly overlap within error and yield mean conditions for the Ertix hanging-wall of 620 ± 50 °C and 6.7 ± 1 kbar. This average is shown with a solid dot in Figure 4.

TABLE 3. MONAZITE ISOTOPIC DATA FOR ALTAI METAPELITE

mount-grain-spot	Monazite location	$^{208}Pb^*/^{232}Th$	Standard Error	Th/U	Percent $^{208}Pb^*$	ThO_2/Th	$^{208}Pb/^{232}Th$ Age ± 1σ
Ertix garnet amphibolite (5b)							
m10-a2	included	0.01263	0.00027	6.879	94.85	2.465	253.6 ± 5.43
m10-d2	matrix	0.01327	0.00019	4.968	98.36	2.646	266.4 ± 3.73
m11-a1	included	0.0133	0.00033	10.25	95.32	2.407	267 ± 6.56
m10-g2	matrix	0.01339	0.00043	11.35	95.16	2.26	268.8 ± 8.53
m11-a2	matrix	0.01345	0.00021	1.788	91.74	3.254	270.1 ± 4.14
m10-e3	included	0.01357	0.00042	11.14	83.33	3.322	272.4 ± 8.39
m10-d1	included	0.0138	0.00018	7.364	95.72	3.023	277 ± 3.66
m11-b2	matrix	0.01431	0.00037	15.06	97.19	2.364	287.3 ± 7.37
m10-a1	matrix	0.01443	0.00011	8.581	98.48	2.945	289.6 ± 2.28
m10-e6	matrix	0.01461	0.00037	4.923	71.13	2.398	293.1 ± 7.28
		Weighted Mean $^{208}Pb/^{232}Th$ Age (2σ)					278 ± 9 Ma, MSWD = 7.8
Calibration†: (0.116 ± 0.009)x + (0.500 ± 0.19); r^2 = 0.997							

Note: MSWD—mean square of weighted deviates.
†Best fit of the calibration to the equation of a line (slope * x + intercept) with ±1σ uncertainty; correlation (r^2).

In Situ Monazite Analyses

The schist with synkinematic garnets (sample 5C) also contained monazite, which we dated using in situ ion-microprobe Th-Pb techniques. Dates of four included and six matrix monazites range from 293 to 254 Ma and have a weighted mean of 278 ± 9 (mean square of weighted deviates [MSWD] = 7.8) (Fig. 5B, Table 3). Monazite grains from both the matrix of the rock and included in garnet during growth have age populations that yield similar weighted mean ages (278 ± 13 Ma and 279 ± 21 Ma, respectively). In the absence of compositional data for the monazites and given the potential age variability suggested by the MSWD, we do not attempt to be more specific than assigning a Permian age for monazite growth.

U-Pb Zircon Geochronology

We present weighted mean ages for zircon analyses that cluster on concordia diagrams assuming negligible Pb-loss and sampling of only a single age domain by the ion beam. Concordia diagrams are shown in Figure 6, while complete isotopic data are available in the GSA Data Repository as Table DR2 (see footnote 1), and grain images are shown in Figure DR4 (see footnote 1).

A series of NNE-striking felsic dikes intrude the Ertix hanging wall. The southern termination of the dikes and the trace of the fault occur within 2–5 m of one another; some of the dikes are clearly truncated by the Ertix fault, suggesting the terminal motion on the fault postdates the dikes (Fig. 2). In addition, the dikes are unmetamorphosed and unfoliated, and so probably intruded after the end of ductile deformation. One such dike, sample 1 in Figure 2, yielded euhedral zircon. Six concordant analyses (Fig. 6A) give a weighted mean age of 286 ± 12 Ma, with a MSWD of 1.9.

Two foliated plutons within the hanging wall of the Ertix fault were analyzed to determine the timing of ductile deformation. The first sample (sample 6) is foliated granite located south of the Ertix river (Fig. 2) and contains brown, equant zircon. Six analyses cluster at ca. 450 Ma on the concordia diagram (Fig. 6A), whereas the other two are younger (ca. 350 Ma). The two younger age analyses are from the same zircon grain, which is dark and featureless in cathode luminescence (CL) imaging, while the older zircon grains exhibit concentric zoning (GSA Data Repository Figure DR4). Moreover, a plot of Th/U versus age reveals that the young grain has distinctly different Th/U ratios compared with the other analyses from this sample (Fig. 7). The weighted mean of the six older analyses is 448 ± 30 Ma (MSWD = 1.6), which we interpret as the emplacement age for this granite.

The Ertix hanging-wall is also intruded by granitoids that lack gneissic foliation. An unfoliated granite (sample 7, Fig. 2) was collected south of the Ertix river. Zircon in the sample is typically euhedral with concentric CL zoning, which echoes the shape of the grains. All concordant analyses cluster at ca. 280 Ma except one, which has an age of 454 Ma (Fig. 6C). Textural evidence is inconclusive about the origin of this analysis: in CL images, the grain is concentrically zoned and no presence of a core was detected. In addition, the geochemistry of the bulk rock and the Th/U of the individual zircon analyses are all consistent with a magmatic origin for the zircons (0.2 ± 0.1; Mahood and Hildreth, 1983). However, based on the geochemistry of this sample (Table 4), the zircon saturation temperature for this rock is 793 °C, which is consistent with the possibility of inherited zircon as shown by Harrison and Watson (1983). In addition, given the ages of the gneiss and foliated pluton samples in the region, ca. 450 Ma is not an unlikely age for an inherited zircon. Aside from the older, probably inherited zircon, twelve analyses have a weighted mean of 278 ± 7 Ma (MSWD = 1.1), which we interpret as the crystallization age for this pluton.

Sample 9a (Fig. 2) is from a large orthogneiss body found in the central region of the Ertix gneiss complex with a NW striking and NE dipping foliation parallel to fabrics in the rest of the gneiss complex. Zircon grains are clear, subhedral to euhedral, and yield a spread in ages from 412 to 478 Ma. However, analyses are concordant, with the exception of three, which lie just above concordia and are likely the result of a slight ^{204}Pb over-correction (Fig. 6D). The weighted mean of all 12 analyses is 451 ± 14 Ma (MSWD = 0.85), which is the oldest age bound for the deformation of the Ertix gneiss complex.

North of the Ertix river, we examined another foliated pluton, sample 10 (Fig. 2), a garnet-bearing trondhjemite. Zircons from this pluton have low U concentrations, and as a consequence, have large 2σ error ellipses (Fig. 6E). Unfortunately, we cannot interpret an age from these analyses, though the data are permissive of an age similar to that of the other gneiss and foliated pluton samples analyzed.

North of the Ertix river, we sampled a tonalitic gneiss (sample 11, Fig. 2). This sample has a complicated zircon population (Fig. 6F). Whereas most of the eight analyses cluster between 433 and 478 Ma, three of the analyses are distinctly younger, yielding ages of ca. 385 Ma, ca. 350 Ma and ca. 270 Ma. We have identified CL-bright, zoned cores and CL-dark rims that correspond to the Ordovician and younger age populations, respectively (GSA Data Repository Figure DR4). The younger analyses, which have slightly lower Th/U ratios (Fig. 7), are potentially related to multiple zircon growth episodes or a single young zircon growth episode that the ion beam sampled in different proportions with older, core portions of the zircon grain during our analysis. Excluding these three CL-dark rim analyses, the weighted mean of the $^{206}Pb/^{238}U$ ages is 451 ± 23 Ma (MSWD = 0.63) and represents the best interpretation of these data assuming negligible Pb-loss and

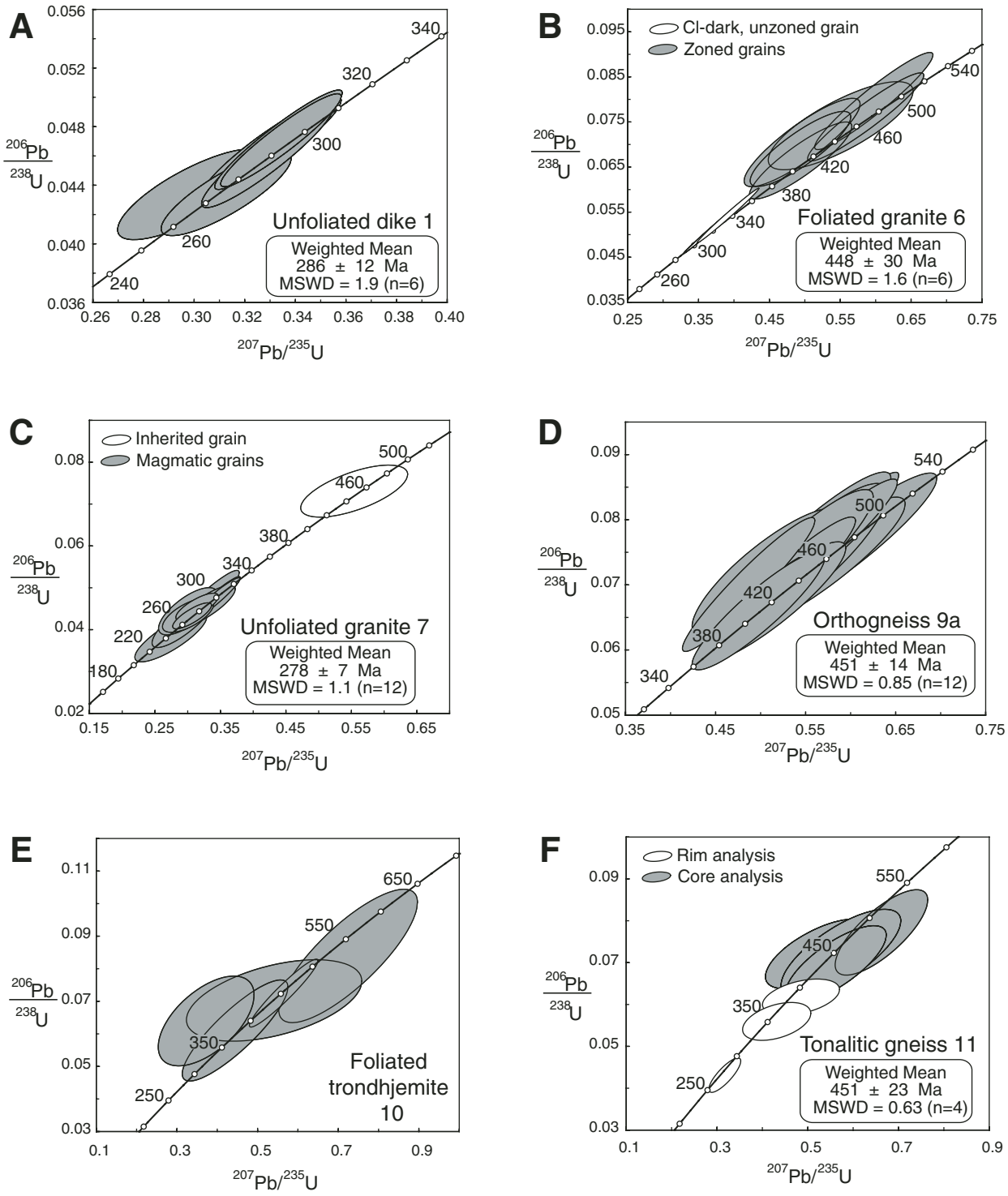

Figure 6. U-Pb concordia diagrams of zircon analyses from Ertix hanging wall. Error ellipses are 2σ; weighted mean of $^{206}Pb/^{238}U$ ages are reported, with analyses marked by white ellipse excluded from weighted mean. (A) Unfoliated granitic dike truncated by the Ertix fault (sample 1). (B) Foliated granite (sample 6). (C) Unfoliated granite (sample 7). D. Orthogneiss (sample 9A). (E) Foliated trondhjemite (sample 10). (F) Tonalitic gneiss (sample 11). MSWD—mean square of weighted deviates.

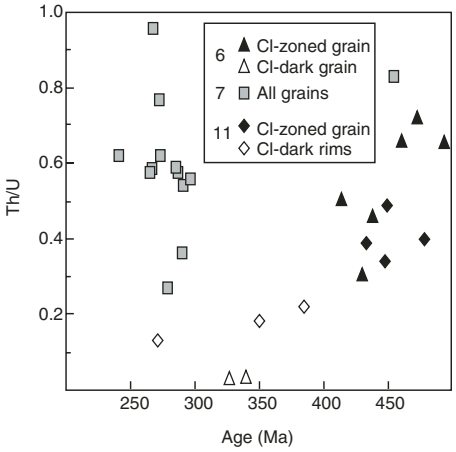

Figure 7. U/Th ratios and ages for zircon analyses from samples 6 (filled and open triangles), 7 (gray filled squares) and 11 (filled and open diamonds). Cl—cathode luminescence.

sampling of only a single age domain by the ion beam.

In summary, our U-Pb dating suggests that the deformed plutons are Ordovician to Devonian and the non-foliated granitoids are Permian in age. A dike cut by the Ertix fault intruded at 286 ± 12 Ma in the early Permian.

$^{40}Ar/^{39}Ar$ Thermochronology

Sample 2, located <10 m north of the Ertix fault (Fig. 2), is a garnet-amphibolite schist that represents the deepest rocks we examined in the Ertix hanging wall. Amphibole yields a disturbed age spectrum for the first 40% of gas released, but 56% of the gas released, corresponding to the heating steps between 1060 °C and 1350 °C, has a weighted mean age of 271 ± 6.6 Ma (Fig. 8). We interpret this as the time at which argon began to be retained within the amphibole (~500 °C; McDougall and Harrison, 1999). A granitic gneiss sample (sample 5a) and a metapelitic schist sample (sample 5c) were collected ~500 m north of the Ertix fault from the Ertix gneiss (location 5 in Fig. 2). $^{40}Ar/^{39}Ar$ analysis of muscovite and biotite from this location yield flat age spectra, with slight disturbances for the first 3%–8% of argon released (Fig. 8). Muscovite from sample 5a has a weighted mean age of 275 ± 8 Ma, while sample 5c yields biotite with a weighted mean age of 259 ± 10 Ma.

Sample 8 is a garnet amphibolite located ~3 km north of the Ertix thrust (Fig. 2). It yields a complex biotite age spectrum with a significant (100 Ma) age gradient over the first several steps (Fig. 8). The total gas age for this sample is 254 ± 8 Ma. Sample 9b is an orthogneiss collected ~4 km north of the fault (Fig. 2). The age spectrum of a K-feldspar from this unit exhibits a flat plateau at ca. 265 Ma, with a slight hump in the spectrum for the first ~20% of gas released (Fig. 8). Biotite from sample 11, a tonalitic gneiss collected 6 km north of the Ertix fault (Fig. 2), displays a concave-down age spectrum similar to sample 8, with a significant age gradient for the first several temperature steps (Fig. 8). It records a total gas age of 270 ± 8 Ma. Biotite from sample 12b, a mafic gneiss 7 km north of the Ertix thrust, yields a monotonically increasing age spectrum. The central plateau, representing ~84% of the gas released, has a weighted mean age of 262 ± 11 Ma and an inverse isochron age of 267 Ma. From the same location, a granitic gneiss, sample 12f (Fig. 2), yields K-feldspar with a flat age spectrum and a weighted mean age of 269 ± 8 Ma. Multi-domain diffusion (MDD) modeling of K-feldspar from sample 12b suggests rapid cooling from 400 °C to 150 °C between 271 and 265 Ma (Fig. 8; Lovera et al., 1997).

DISCUSSION

Magmatism

U-Pb zircon results from six igneous and meta-igneous bodies in the hanging wall of the Ertix fault indicate two periods of magmatism. The first is latest Ordovician (ca. 451–433 Ma) and is recorded in rocks identified in the field as gneisses and foliated plutons (i.e., samples 6, 9b, 10, and 11). Some of these samples do yield younger age analyses, which are potentially related to later metamorphic zircon growth (e.g., sample 11). An unfoliated granite and a granitic dike were intruded into the Ertix hanging-wall metamorphic rocks in the Permian (ca. 278–286 Ma). Bulk rock geochemistry of four of the samples is consistent with arc magmatism when plotted on geochemical discrimination diagrams (Fig. 9; e.g., Pearce et al., 1984). For the Permian granite (sample 7), our geochemical results suggest an arc origin that is incompatible with the early interpretation of anorogenic granites for late Paleozoic magmatism (e.g., Coleman, 1989). More germane to the aim of this study, however, is that these two periods of magmatism have bracketed the time of ductile deformation to post-Ordovician and pre-Permian and that the age of the granitic dike cut by the Ertix fault suggests that termination of slip on the Ertix had to occur after ca. 286 Ma.

Deformation History

Kinematic indicators such as down-dip striations, cleavage in fault gouge zones, fold hinges, and S-C fabrics from the Ertix fault in the Chinese Altai are consistent with SW-directed thrusting. Additionally, our results indicate that variations in fault strike may reconcile some of the conflicting shear sense indicators previously reported along the Ertix fault zone (e.g., Mileyev et al., 1980; Qu and Zhang, 1994; Mitrokhin et al., 1997). The sharp break in metamorphic grade across the Ertix fault also supports significant vertical juxtaposition of the crustal section and is consistent with thrust kinematics. Assuming a crustal density equal to that of average continental crust (2800 kg/m^3), the resulting lithostatic pressure gradient (~2.7 kbar/km) would suggest burial depths of 25 km based on the calculated peak pressure of ~6.7 kbar. However, the unmetamorphosed to low-grade rocks in the footwall were likely buried to no more than 10–15 km, so that the Ertix fault was responsible for at least 10–15 km of vertical motion.

Quantitative thermobarometry of four samples indicates peak pressures and temperatures of 6.2–7.7 kbar and 560–670 °C for the hanging wall of the Ertix thrust. Previous workers have suggested the presence of an inverted metamorphic gradient in the Ertix hanging wall (Yang et al., 1992; Qu and Zhang, 1994). Broadly, the relative differences in *P* and *T* between the three locations in our study may indicate that structurally higher samples record higher conditions, but the small sample size and low precision of the results do not allow a full exploration of the inverted-metamorphism hypothesis.

Monazite appears in a metapelitic schist near the garnet-in isograd. Th-Pb ages of this mineral are typically interpreted as representing the time of monazite growth at or near peak metamorphic temperatures. However, multiple reactions produce the phase at different temperatures and often yield complicated zoning textures at the grain scale (Catlos et al., 2002; Pyle and Spear, 2003; Kohn et al., 2004, 2005). In this study, the weighted mean of the monazite ages (278 ± 9 Ma) is 6 m.y. older than the muscovite age at the same outcrop, and some monazite analyses are apparently younger than muscovite and biotite ages. In addition, one garnet-included monazite yields an age younger than most matrix monazite (Fig. 5). While the diffusivity of Pb in monazite is too low to disturb the Th-Pb systematics even at peak temperatures (Cherniak et al., 2004), the garnets in this sample are cracked and are riddled with poly-mineralic inclusions. It is plausible, therefore, that either some monazite recrystallized during retrograde metamorphism within the garnets and/or experienced some fluid-driven dissolution or reprecipitation at temperatures lower than those recorded by the thermobarometry (e.g., Wing et al., 2003; Ayers

et al., 2006). Given the reconnaissance nature of these ages, and the potential inaccuracies introduced by the choice of standards and associated calibrations, we interpret the Permian monazite ages as representing the youngest bound on high-grade metamorphism.

Results from $^{40}Ar/^{39}Ar$ are variable, but some useful information is preserved. The amphibole release spectrum is significantly disturbed, but a plateau suggests cooling through 500 °C at 271 ± 7 Ma, while a muscovite analysis has an age of 275 ± 8 Ma. Of the four biotite spectra, the most disturbed have low potassium contents, seen in low equivalent K_2O% values calculated from step heating data. This is likely the result of impurity or alteration, and we take the more robust biotite analyses (samples 8 and 12b) to generally indicate cooling through biotite closure at 260 ± 10 Ma. Two K-feldspars display similar spectra consistent with cooling at 267 ± 8 Ma. Furthermore, multi-domain diffusion modeling of K-feldspar indicates rapid cooling (>25 °C/m.y.) between 270 and 265 Ma. In detail, the argon ages show no systematic variation across the Ertix hanging wall. This is contrary to the simple case of thrust motion (e.g., McDougall and Harrison, 1999), but the lack of a preserved age gradient could result from the low spatial resolution of this study or internal deformation of the Ertix thrust sheet (e.g., Robinson, 2005). All together, these data indicate that the rocks of the Ertix hanging wall cooled from >500 °C to 150 °C from ca. 275 to 265 Ma. Since we also observe Permian magmatism in the Ertix hanging wall, the possibility exists that these mica ages result from the conductive cooling of plutons in the region rather than tectonic exhumation. However, the limited extent of exposure of undeformed granitic bodies at the surface in the hanging wall compared with the >10 km across strike extent of the cooling signal makes this unlikely. In addition, these cooling age results are consistent with other $^{40}Ar/^{39}Ar$ results in both China (Laurent-Charvet et al., 2003) and Kazakhstan (Vladimirov et al., 1997; Travin, et al., 2001) along the Ertix fault zone. Finally, the age of a dike cut by the Ertix fault (sample 1) suggests slip on the structure after 286 ± 12 Ma. Therefore, we interpret this cooling as resulting from tectonic uplift of these rocks along the Ertix thrust fault coupled with erosion at the surface.

Timing and Estimated Slip Rates on the Ertix Fault

Combined argon results indicate that the Ertix hanging-wall rocks cooled from ≥500 °C to ~150 °C during the Permian, between 275 and 265 Ma (Fig. 10). The calculated cooling rate from these results is 35 °C/m.y. If we used the

TABLE 4. GEOCHEMICAL DATA FOR SELECTED GRANITOIDS

Sample:	11	6	10	7
Description†:	Tonalitic gneiss	Foliated granite	Foliated trondhjemite	Unfoliated granite
SiO_2	64.46	76.48	72.77	72.19
TiO_2	0.343	0.126	0.121	0.284
Al_2O_3	16.10	12.04	15.20	14.11
Fe_2O_3§	4.61	1.25	1.06	2.36
MnO	0.107	0.016	0.072	0.048
MgO	1.70	0.12	0.34	0.59
CaO	5.32	0.49	2.31	2.28
Na_2O	4.01	3.53	5.77	3.55
K_2O	1.06	4.55	0.99	3.30
P_2O_5	0.14	0.03	0.05	0.13
LOI	1.23	0.54	0.74	0.76
TOTAL	99.08	99.17	99.41	99.59
Ab	35.60	27.65	49.17	30.70
An	22.30	0.00	6.26	8.40
Or	6.88	27.32	6.29	20.11
M factor	1.76	1.33	1.43	1.41
T_{sat} °C	706	779	684	793
Rb	13	81	7	107
Sr	548	73	523	215
Ba	493	476	587	541
Zr	72	140	53	169
Nb	3.0	8.1	3.0	8.2
Hf	2.3	7.1	1.6	5.2
Ta	1.96	1.85	1.58	1.70
Th	0.72	18.5	0.48	15.6
U	0.14	3.23	0.13	3.58
Cs	0.3	0.3	0.1	1.7
Y	11.3	17.5	5.6	26.7
Pb	6	10	–#	17
Ag	–	–	–	–
V	81	6	–	21
Cr	–	–	–	–
Co	130	92	90	57
Ni	–	–	–	–
Cu	14	29	–	–
La	6.40	20.8	6.58	31.7
Ce	12.6	42.2	12.0	62.6
Pr	1.71	5.01	1.45	7.17
Nd	7.43	18.4	5.67	27.0
Sm	1.74	3.60	1.08	5.24
Eu	0.663	0.328	0.437	1.03
Gd	1.90	3.28	0.96	5.13
Tb	0.30	0.50	0.13	0.78
Dy	1.88	3.05	0.81	4.61
Ho	0.38	0.59	0.18	0.88
Er	1.26	1.97	0.65	2.78
Tm	0.193	0.331	0.116	0.446
Yb	1.29	2.17	0.88	2.76
Lu	0.237	0.380	0.167	0.470
Th/U	5.035	5.730	3.634	4.352
Zn	41	–	–	–
Ga	14	12	12	15
Ge	1.3	1.0	1.0	1.1
As	–	–	–	–
Mo	2	2	–	–
In	–	–	–	–
Sn	5	5	5	4
Sb	–	–	–	–
W	1,360	1,250	1,230	645
Tl	0.07	0.40	–	0.81
Bi	–	–	–	–

†From Barker (1979).
§All iron as Fe_2O_3.
#Not detected at the lower limit.

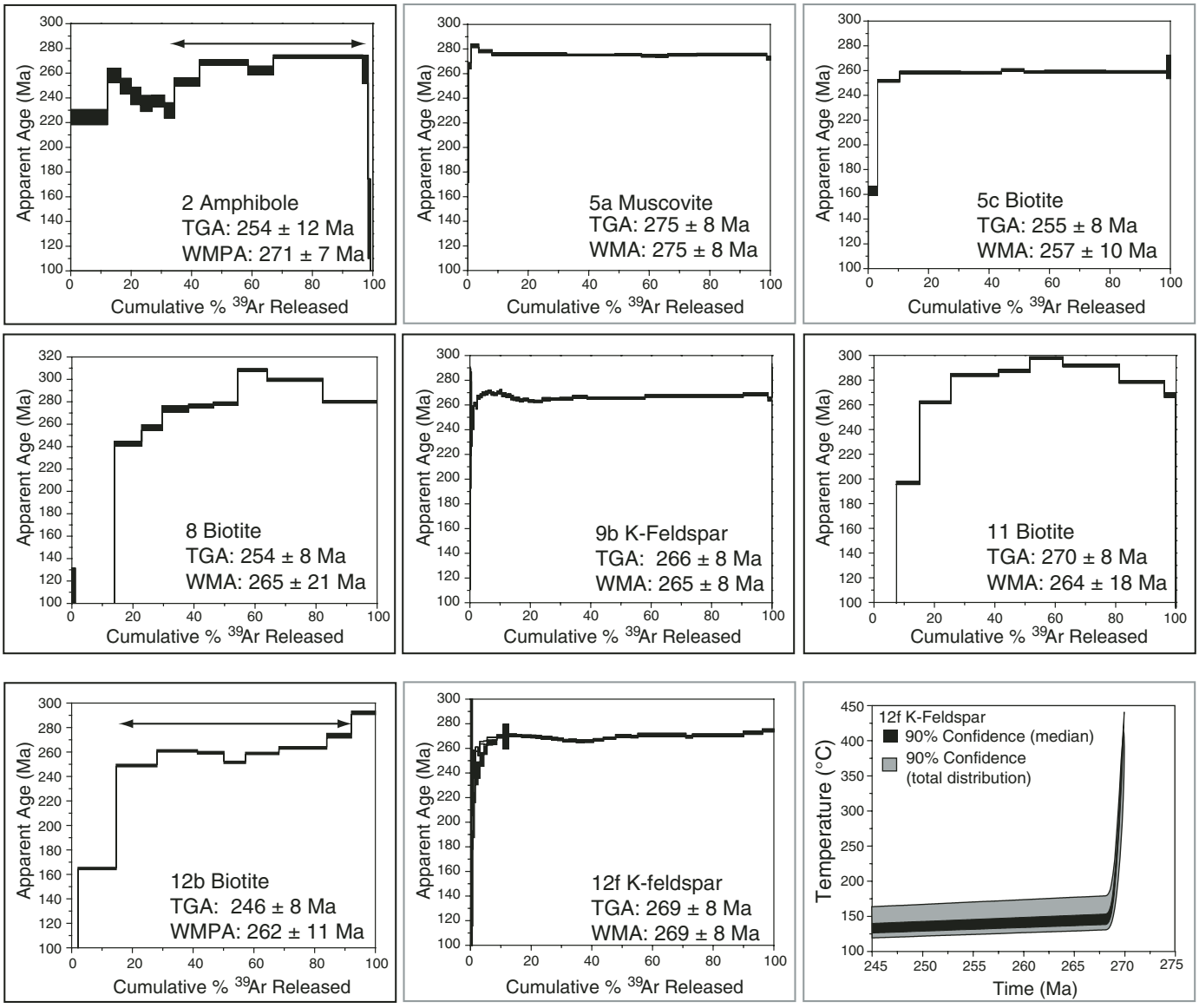

Figure 8. $^{40}Ar/^{39}Ar$ release spectra and thermal history from multi-domain diffusion–modeling for the Ertix gneiss complex, labeled with sample number and phase. In some cases, arrows indicate portion of plateau used for weighted mean plateau age. TGA—total gas age; WMA—weighted mean age; WMPA—weighted mean plateau age.

weighted mean monazite age as a reliable indicator of the timing of peak metamorphic temperatures of ~620 °C, and combine this information with the argon data, the calculated cooling rate is 36.3 °C/m.y. Given that peak metamorphism could be older than the age recorded by the monazite data, this is a maximum cooling rate. Assuming a 20 °C/km geothermal gradient, this would suggest a vertical exhumation rate of 1.75 mm/yr (argon data only) or 1.82 mm/yr (monazite and argon data). Taking an erosion rate of 1 mm/yr, and using a fault dip of 55°, the Permian slip rate on the Ertix fault would be 0.9 mm/yr (monazite neglected) to 1 mm/yr (with monazite data).

Origin of the Ertix Gneiss Complex and Tectonic Reconstruction

The Ertix gneiss complex was considered to be Precambrian basement (e.g., He et al., 1990). However, our geochronological studies so far do not support this hypothesis. Although Pb-Pb feldspar model ages and Pb-Pb zircon analyses have been interpreted to indicate the presence of Precambrian crust (e.g., Qu and Chong, 1991; Windley et al., 2002), whether the older zircons are from Precambrian igneous rocks or detritus transported to an Early Ordovician accretionary wedge and later intruded by latest Ordovician plutons remain unclear. However, one of the important observations made by this and earlier studies about the Ertix gneiss complex is that it consists of significant components of oceanic assemblages, including metachert, metabasite, and locally ultramafic rocks. Although lithologically one may interpret these rocks as a mélange complex (e.g., O'Hara et al., 1997), the temperature conditions are too high for those typically expected in a subduction zone setting (e.g., Peacock and Wang, 1999). To resolve this paradox, we propose that the Ertix gneiss complex originated from an accretionary mélange but had been modified by tectonic burial and possibly later arc magmatism in the Early Permian. This explains why the mélange materials were exhumed from

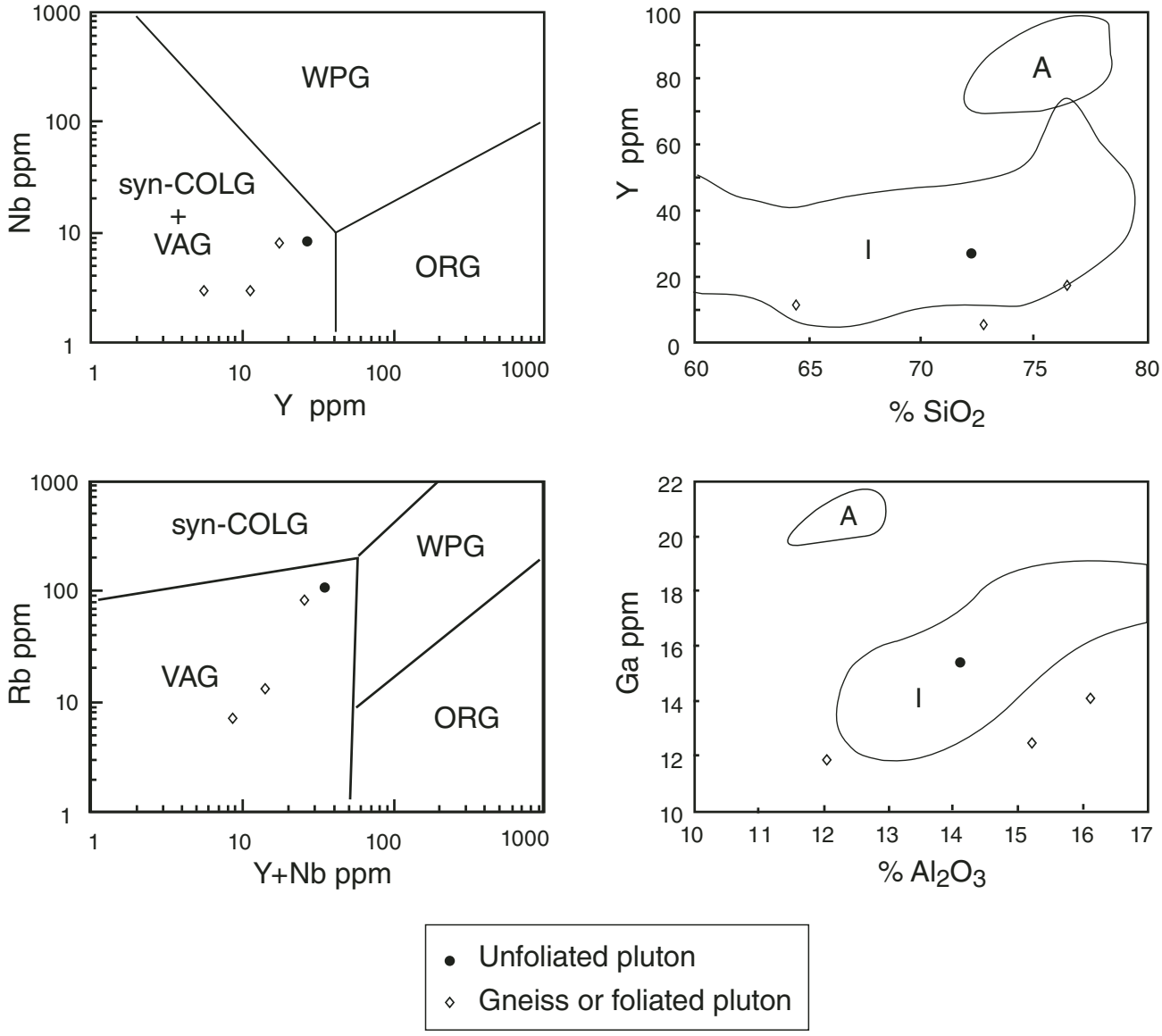

Figure 9. Geochemical discrimination diagrams, after Pearce et al. (1984) and Collins et al. (1982). Fields labels: A—A-type granites; I—I-type granites; ORG—ocean ridge granites; syn-COLG—syn-collision granites; VAG—volcanic arc granites; WPG—within-plate granites.

lower crustal depths and are now exposed within an arc, with Paleozoic igneous components in both the Ertix hanging wall and footwall.

TECTONIC MODEL FOR THE EVOLUTION OF THE CHINESE ALTAI

In order to explain the timing of igneous activity and deformation in the Chinese Altai, we propose the following tectonic history (Fig. 11). First, we suggest a Cambro-Ordovician arc that developed over the Altai region above a south-dipping subduction zone (Fig. 11A). The development of this arc has also been documented in the Valley of Lakes region in western Mongolia by Badarch et al. (2002). The Junggar ocean south and west of the Altai arc (in the present geographic coordinates) may have been expanding by mid-oceanic-ridge spreading but probably did not subduct below the Altai arc (Fig. 11A). A Devonian arc developed within the southern margin of the Junggar oceanic plate due to northward subduction of the Tarim plate (Windley et al., 1990) (Fig. 11B). This arc, now located in the northern Tian Shan in western China, eventually collided with, and obducted onto, the Tarim craton in the Late Carboniferous (Carroll et al., 1995). To the north, collision of the Cambro-Ordovician Altai arc over the Altai region with either a microcontinent (the central Mongolia microcontinent of Badarch et al., 2002) or the southern margin of the Siberian continent may have terminated magmatism and created a magmatic hiatus throughout the Late Devonian and Carboniferous in the Chinese Altai region (Fig. 11B). Northward subduction of the Junggar plate below the Altai initiated in the Late Carboniferous and lasted until the Early Permian (Figs. 11C and 11D). During this period, a mélange complex developed along the southern margin of the Altai arc; it was later subducted and emplaced at the base of the Altai arc. Contractional deformation and thrusting along the Ertix fault during the Early Permian was responsible for carrying the

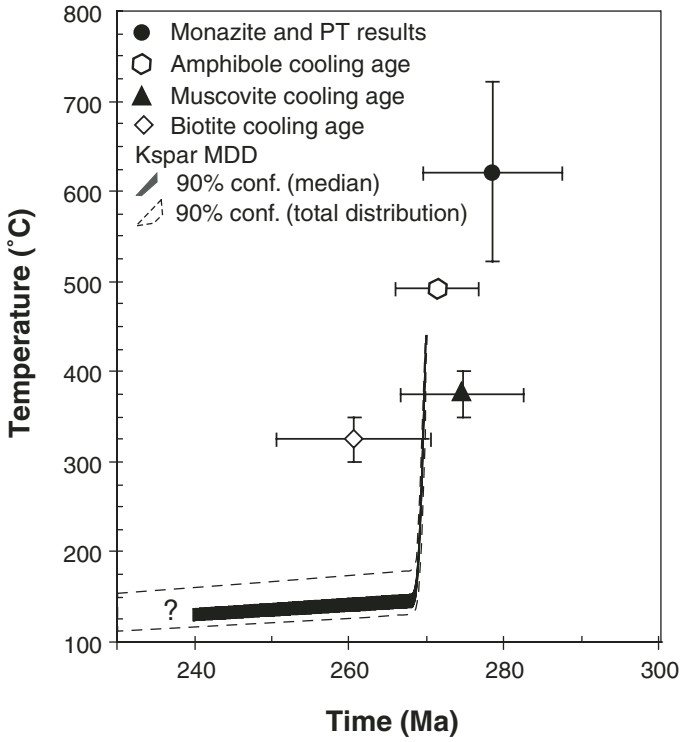

Figure 10. Combined temperature-time diagram for hanging-wall rocks of the Ertix fault. PT—temperature estimate from quantitative thermobarometry. Kspar MDD—thermal history from K-feldspar multi-domain diffusion modeling.

high-grade mélange complex to shallow crustal levels (Fig. 11E). Initiation and subsequent motion on the Ertix fault was coeval with intrusion of Permian granitoids, suggesting that this fault was developed within an intra-arc setting during oceanic subduction.

CONCLUSIONS

Our integrated structural, geochronological, thermochronological, and petrological studies have shed new light on the kinematics and timing of the Ertix fault, a dominant structure in the Central Asian Orogenic System. We conclude that the Ertix fault is a major crustal-scale thrust that has carried rocks from lower crustal depths to shallow crustal levels in the late Paleozoic between ca. 290 and 265 Ma. As a result, the fault currently juxtaposes amphibolite-grade rocks over unmetamorphosed to lower greenschist-facies rocks in the Chinese Altai. Two phases of igneous activities have been detected by our geochronological studies. The first phase occurred ca. 450 Ma in the latest Ordovician and the second phase occurred ca. 280 Ma. The Permian intrusions are cut by the Ertix fault, indicating that motion on the fault did not terminate before 280 Ma. This is consistent with our inferred duration of faulting (275–265 Ma) based on the cooling history of rocks in the Ertix hanging wall.

In the context of regional geology, we suggest that the Chinese–Mongolia Altai has experienced two phases of subduction: one in the Ordovician-Devonian and another during the Late Carboniferous to Early Permian. A hiatus of ~100 m.y. between 380 and 280 Ma occurred between the two phases of arc magmatism. The high-grade assemblage of the Ertix hanging wall, consisting of metabasite, metachert, and deformed granites, may be best explained as a result of tectonic burial and emplacement of a mélange complex below an arc.

ACKNOWLEDGEMENTS

Detailed reviews by Elizabeth Catlos, Brent Miller, and associate editor Matt Kohn significantly improved this manuscript. We thank Frank Kyte for assistance with the electron microprobe analysis, Axel Schmitt for help with the ion microprobe, and Kurt Frankel for reading earlier versions of this manuscript. The University of California at Los Angeles ion microprobe facility is supported in part by a grant from the Instrumentation and Facilities Program, Division of Earth Sciences, National Science Foundation. An Yin's research in Asia has been supported by the Tectonics Program, National Science Foundation.

REFERENCES CITED

Allen, M.B., Windley, B.F., and Chi, Z., 1993, Palaeozoic collisional tectonics and magmatism of the Chinese Tien Shan, central Asia: Tectonophysics, v. 220, p. 89–115, doi: 10.1016/0040-1951(93)90225-9.

Allen, M.B., Şengör, A.M.C., and Natal'in, B.A., 1995, Junggar, Turfan and Alakol Basins as Late Permian to Early Triassic extensional structures in a sinistral shear zone in the Altaid Orogenic Collage, Central-Asia: Journal of the Geological Society (London), v. 152, p. 327–338.

Ayers, J.C., Loflin, M., Miller, C.F., Barton, M.D., and Coath, C.D., 2006, In situ oxygen isotope analysis of monazite as a monitor of fluid infiltration during contact metamorphism: Birch Creek Pluton aureole, White mountains, eastern California: Geology, v. 34, p. 653–656, doi: 10.1130/G22185.1.

Badarch, G., Cunningham, D., and Windley, B.F., 2002, A new terrane subdivision for Mongolia: Implications for the Phanerozoic crustal growth of Central Asia: Journal of Asian Earth Sciences, v. 21, no. 1, p. 87–110, doi: 10.1016/S1367-9120(02)00017-2.

Barker, F., 1979, Trondhjemite; definition, environment and hypotheses of origin, *in* Barker, F., ed., Trondhjemites, dacites, and related rocks: Amsterdam, Elsevier, p. 1–12.

Bullen, M.E., Burbank, D.W., Garver, J.I., and Abdrakhmatov, K.Y., 2001, Late Cenozoic tectonic evolution of the northwestern Tien Shan: New age estimates for the initiation of mountain building: Geological Society of America Bulletin, v. 113, p. 1544–1559, doi: 10.1130/0016-7606(2001)113<1544:LCTEOT>2.0.CO;2.

Buslov, M.M., Watanabe, T., Fujiwara, Y., Iwata, K., Smirnova, L.V., Safonova, I.Y., Semakov, N.N., and Kiryanova, A.P., 2004, Late Paleozoic faults of the Altai region, Central Asia: tectonic pattern and model of formation: Journal of Asian Earth Sciences, v. 23, no. 5, p. 655–671, doi: 10.1016/S1367-9120(03)00131-7.

Carroll, A.R., Graham, S.A., Hendrix, M.S., Ying, D., and Zhou, D., 1995, Late Paleozoic tectonic amalgamation of northwestern China: Sedimentary record of the northern Tarim, northwestern Turpan, and southern Junggar basins: Geological Society of America Bulletin, v. 107, p. 571–594, doi: 10.1130/0016-7606(1995)107<0571:LPTAON>2.3.CO;2.

Catlos, E.J., Gilley, L.D., and Harrison, T.M., 2002, Interpretation of monazite ages obtained via in situ analysis: Chemical Geology, v. 188, p. 193–215, doi: 10.1016/S0009-2541(02)00099-2.

Cebula, G.T., Kunk, M.J., Mehnert, H.H., Naeser, C.W., Obradovich, J.D., and Sutter, J.F., 1986, The Fish Canyon Tuff, a potential standard for the ^{40}Ar-^{39}Ar and fission-track dating methods: Terra Cognita, v. 6, p. 139–140.

Chen, B., and Jahn, B.M., 2002, Geochemical and isotopic studies of the sedimentary and granitic rocks of the Altai orogen of northwest China and their tectonic implications: Geological Magazine, v. 139, p. 1–13, doi: 10.1017/S0016756801006100.

Chen, B., and Jahn, B.M., 2004, Genesis of post-collisional granitoids and basement nature of the Junggar terrane, NW China: Nd-Sr isotope and trace element evidence: Journal of Asian Earth Sciences, v. 23, p. 691–703, doi: 10.1016/S1367-9120(03)00118-4.

Cherniak, D.J., Watson, E.B., Grove, M., and Harrison, T.M., 2004, Pb diffusion in monazite: A combined RBS/SIMS study: Geochimica et Cosmochimica Acta, v. 68, no. 4, p. 829–840, doi: 10.1016/j.gca.2003.07.012.

Chikov, B.M., Zinov'ev, S.V., and Podtsibastenkova, E.A., 1988, Morphological types of flow structures in the blastomylonites of the Irtysh crumpling zone: Geology and Geophysics, v. 29, p. 11–14.

Coleman, R.G., 1989, Continental growth of northwest China: Tectonics, v. 8, p. 621–635.

Collins, W.J., Beams, S.D., White, A.J.R., and Chappell, B.W., 1982, Nature and origin of A-type granites with particular reference to southeastern Australia: Contributions to Mineralogy and Petrology, v. 80, p. 189–200.

Corfu, F., 1988, Differential response of U-Pb system in coexisting accessory minerals, Winnipeg River Subprovince, Canadian Shield: Implications for Archean crustal growth and stabilization: Contributions to Mineralogy and Petrology, v. 98, p. 312–325, doi: 10.1007/BF00375182.

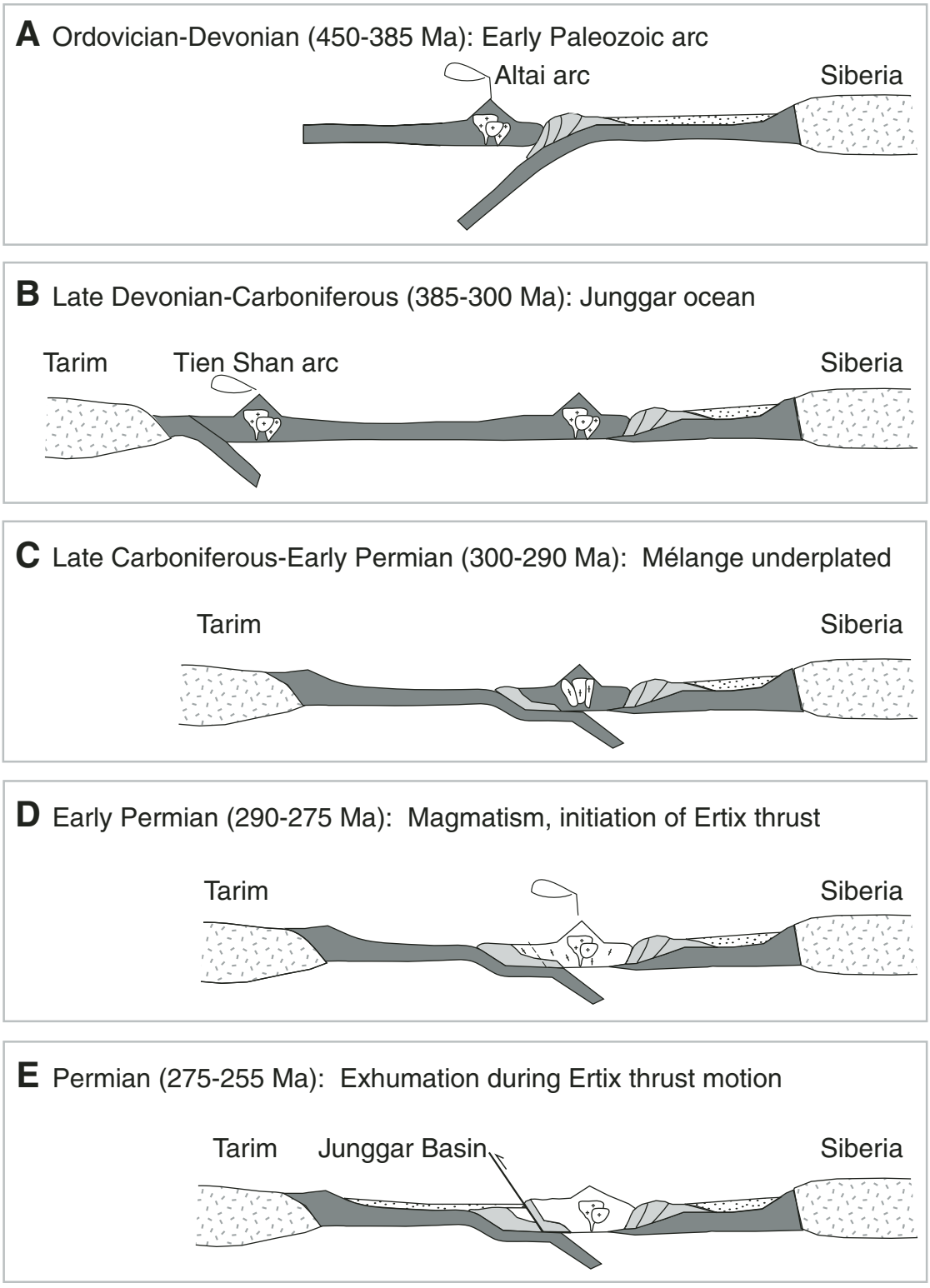

Figure 11. Reconstruction of the Ertix fault and Ertix gneiss complex. North is on the right side of each diagram and shown with the southern margin of material accreted to the Siberian craton before the Ordovician. (A) The Altai Ordovician-Devonian arc and mélange formed during southward dipping subduction of the Junggar oceanic crust. (B) Denudation and erosion of early Paleozoic arc into neighboring basins. (C) Portions of the Altai arc and mélange were underplated and metamorphosed during convergence and closure of the Junggar ocean basin. (D) Permian magmatism intrudes dike complex and other granitoids. (E) Continued slip on Ertix fault leads to exhumation and cooling of the mélange-arc complex.

Cunningham, W.D., Windley, B.F., Dorjnamjaa, D., Badamgarov, G., and Saandar, M., 1996, A structural transect across the Mongolian Western Altai: Active transpressional mountain building in central Asia: Tectonics, v. 15, p. 142–156, doi: 10.1029/95TC02354.

Dale, J., Holland, T., and Powell, R., 2000, Hornblende-garnet-plagioclase thermobarometry: A natural assemblage calibration of the thermodynamics of hornblende: Contributions to Mineralogy and Petrology, v. 140, p. 353–362, doi: 10.1007/s004100000187.

Delvaux, D., Buslov, M.M., Dehandschutter, B., Theunissen, K., and Melnikov, A., 1998, Kinematic and stress field of late Paleozoic strike-slip faulting in Altai-Sayan: Constraints for tectonic models *in* Jahn, B.M., ed. Continental growth in the Phanerozoic: evidence from east-central Asia: IGCP 480 Conference Abstract Volume Abstract Volume, p. 8.

Dobretsov, N.L., Berzin, N., and Buslov, M.M., 1995, Opening and tectonic evolution of the paleo-Asian Ocean: International Geology Review, v. 37, p. 335–360.

Harrison, T.M. and Watson, E.B., 1983, Kinetics of zircon dissolution and zirconium diffusion in granitic melts of variable water content: Contributions to Mineralogy and Petrology, v. 84, p. 66–72.

Harrison, T.M., McKeegan, K.D., and Le Fort, P., 1995, Detection of inherited monazite in the Manaslu leucogranite by $^{208}Pb/^{232}Th$ ion microprobe dating: Crystallization age and tectonic significance: Earth and Planetary Science Letters, v. 133, p. 271–282.

He, G., Han, B.F., Yue, Y., and Wang, J., 1990, Tectonic division and crustal evolution of Altay Orogenic Belt in China: Geoscience of Xinjiang, v. 2, p. 9–20.

Holland, T., and Powell, R., 1998, An internally consistent thermodynamic dataset for phases of petrological interest: Journal of Metamorphic Geology, v. 16, p. 309, doi: 10.1111/j.1525-1314.1998.00140.x.

Hendrix, M.S., Graham, S.A., Amory, J.Y., and Badarch, G., 1996, Noyon Uul syncline, southern Mongolia: Lower Mesozoic sedimentary record of the tectonic amalgamation of central Asia: Geological Society of America Bulletin, v. 108, p. 1256–1274, doi: 10.1130/0016-7606(1996)108<1256:NUSSML>2.3.CO;2.

Jahn, B.M., 2004, The Central Asian Orogenic Belt and growth of the continental crust in the Phanerozoic *in* Malpas, J., Fletcher, C.J.N., Ali, J.R. and Aitchison, J.C. eds., Aspects of the Tectonic Evolution of China: London, The Geological Society, p. 73–100.

Kohn, M.J., and Spear, F., 2000, Retrograde net transfer reaction insurance for pressure-temperature estimates: Geology, v. 28, p. 1127–1130, doi: 10.1130/0091-7613(2000)28<1127:RNTRIF>2.0.CO;2.

Kohn, M.J., Wieland, M.S., Parkinson, C.D., and Upreti, B.N., 2004, Miocene faulting at plate tectonic velocity in the Himalaya of central Nepal: Earth and Planetary Science Letters, v. 228, p. 299–310, doi: 10.1016/j.epsl.2004.10.007.

Kohn, M.J., Wieland, M.S., Parkinson, C.D., and Upreti, B.N., 2005, Five generations of monazite in Langtang gneisses: Implications for chronology of the Himalayan metamorphic core: Journal of Metamorphic Geology, v. 23, p. 399–406, doi: 10.1111/j.1525-1314.2005.00584.x.

Kretz, R., 1983, Symbols for rock-forming minerals: The American Mineralogist, v. 68, p. 277–279.

Lamb, M.A., Hanson, A.D., Graham, S.A., Badarch, G., and Webb, L.E., 1999, Left-lateral sense offset of Upper Proterozoic to Paleozoic features across the Gobi Onon, Tost, and Zuunbayan faults in southern Mongolia and implications for other central Asian faults: Earth and Planetary Science Letters, v. 173, p. 183–194.

Laurent-Charvet, S., Charvet, J., Shu, L., Ma, R., and Lu, H., 2002, Palaeozoic late collisional strike-slip deformations in Tianshan and Altay, Eastern Xinjiang: NW China: Terra Nova, v. 14, no. 4, p. 249–256, doi: 10.1046/j.1365-3121.2002.00417.x.

Laurent-Charvet, S., Charvet, J., Monie, P., and Shu, L.S., 2003, Late Paleozoic strike-slip shear zones in eastern central Asia (NW China): New structural and geochronological data: Tectonics, v. 22, no. 2, p. 1009, doi: 10.1029/2001TC901047, doi: 10.1029/2001TC901047.

Li, T.D., 1997, Geological map of Asia and Europe: Chinese Academy of Geological Sciences, scale 1:5,000,000, 9 sheets.

Liu, W., and Fei, P.X., 2006, Methane-rich fluid inclusions from ophiolitic dunite and post-collisional mafic-ultramafic intrusion: The mantle dynamics underneath the Palaeo-Asian Ocean through to the post-collisional period: Earth and Planetary Science Letters, v. 242, p. 286–301.

Lovera, O.M., Grove, M., Harrison, T.M., and Mahon, K.I., 1997, Systematic analyses of K-feldspar $^{40}Ar/^{39}Ar$ step-heating experiments 1: Significance of activation energy determinations: Geochimica et Cosmochimica Acta, v. 61, p. 3171–3192, doi: 10.1016/S0016-7037(97)00147-6.

Lyons, J.J., Coe, R.S., Zhao, X.X., Renne, P.R., Kazansky, A.Y., Izokh, A.E., Kungurtsev, L.V., and Mitrokhin, D.V., 2002, Paleomagnetism of the early Triassic Semeitau igneous series, eastern Kazakstan: Journal of Geophysical Research, v. 107, doi: 10.1029/2001JB000521.

McDougall, I. and Harrison, T.M., 1999, Geochronology and Thermochronology by the $^{40}Ar/^{39}Ar$ Method: New York, Oxford University Press, 269 p.

Mahood, G., and Hildreth, W., 1983, Large partition coefficients for trace elements in high-silica rhyolites: Geochimica et Cosmochimica Acta, v. 47, p. 11–30, doi: 10.1016/0016-7037(83)90087-X.

Mileyev, V.S., Rotarash, I.A., and Samygin, S.G., 1980, The Irtysh crush belt: Doklady Adademii Nauk SSSR, v. 255, no. 2, p. 413–416.

Mitrokhin, D., Zazansky, A., Theunissen, K., and Berzin, N., 1997, Paleomagnetic and kinematic characteristics of the Irtysh shear zone near Predgornoye (East Kazakhstan): Preliminary Results: Royal Museum of Central Africa, Annual Report, v. 1995 and 1996, p. 187–201.

O'Hara, K.D., Yang, X., Xie, G., and Li, Z., 1997, Regional $\delta^{18}O$ gradients and fluid-rock interaction in the Altay accretionary complex, northwest China: Geology, v. 25, p. 443–446, doi: 10.1130/0091-7613(1997)025<0443:ROGAFR>2.3.CO;2.

Paces, J.B., and Miller, J.D., 1993, Precise U-Pb age of the Duluth Complex and related mafic intrusions, northeastern Minnesota: Geochronological insights in physical, petrogenetic, paleomagnetic, and tectonomagmatic processes associated with the 1.1 Ga midcontinent rift system: Journal of Geophysical Research, v. 98, p. 13,997–14,013.

Peacock, S.M, and Wang, K.L., 1999, Seismic consequences of warm versus cool subduction metamorphism: Examples from southwest and northeast Japan: Science, v. 29, p. 937–939.

Pearce, J.A., Harris, N.B.W., and Tindle, A.G., 1984, Trace element discrimination diagrams for the tectonic interpretation of granitic rocks: Journal of Petrology, v. 25, p. 956–983.

Pyle, J.M., and Spear, F.S., 2003, Four generations of accessory-phase growth in low-pressure migmatites from SW New Hampshire: The American Mineralogist, v. 88, p. 338–351.

Qu, G., and Zhang, J., 1994, Oblique thrust systems in the Altay Orogen, China: Journal of Southeast Asian Earth Sciences, v. 9, p. 277–287, doi: 10.1016/0743-9547(94)90035-3.

Qu, G.S., and Chong, M.Y., 1991, Lead isotopic geology and its tectonic implications in the Altaides, China: Geoscience of Xinjiang, v. 5, p. 100–110.

Quidelleur, X., Grove, M., Lovera, O.M., Harrison, T.M., Yin, A., and Ryerson, F.J., 1997, Thermal evolution and slip history of the Renbu Zedong Thrust, southeastern Tibet: Journal of Geophysical Research, v. 102, B2, p. 2659–2679, doi: 10.1029/96JD02483.

Renne, P.R., Deino, A.L., Walter, R.C., Turrin, B.D., Swisher, C.C., Becker, T.A., Curtis, G.H., Sharp, W.D., and Jaouni, A.R., 1994, Intercalibration of astronomical and radioisotopic time: Geology, v. 22, p. 783–786, doi: 10.1130/0091-7613(1994)022<0783:IOAART>2.3.CO;2.

Robinson, A.C., 2005, Tectonic Evolution of the Konger-Shan normal fault system, Pamir [Ph.D. thesis]: Los Angeles, University of California, 297 p.

Rotarash, A.I., Samygin, S.G., and Gredyushko, A.Y., Keyl'man, G.A., Mileyev, V.S. and Perfil'yev, A.S., 1982, The Devonian active continental margin in the southwestern Altay: Geotectonics, v. 16, no. 1, p. 31–41.

Şengör, A.M.C., and Natal'in, B.A., 1996, Paleotectonics of Asia: fragments of a synthesis, *in* Yin, A., and Harrison, T.M., eds., The Tectonic Evolution of Asia: New York, Cambridge University Press, p. 486–640.

Şengör, A.M.C., Natal'in, B.A., and Burtman, V.S., 1993, Evolution of the Altaid Tectonic Collage and Paleozoic Crustal Growth in Eurasia: Nature, v. 364, no. 6435, p. 299–307, doi: 10.1038/364299a0.

Tapponnier, P. and Molnar, P., 1979, Active faulting and Cenozoic tectonics of the Tien Shan, Mongolia, and Baykal regions: Journal of Geophysical Research, v. 84, p. 3425–3459.

Travin, A.V., Vladimirov, V.G., and Boven, A., 2001, Implication of $^{40}Ar/^{39}Ar$ data on the tectonothermal evolution of the Irtysh shear zone (Eastern Kazakhstan): *in* Jahn, B.M., ed., Continental growth in the Phanerozoic: evidence from central Asia: IGCP 480 Conference Abstract Volume, p. 106–107.

Vladimirov, A.G., Ponomareva, A.P., Shokalskii, S.P., Khalilov, V.A., Kostitsyn, Y.A., Ponomarchuk, V.A., Rudnev, S.N., Vystavnoi, S.A., Kruk, N.N., and Titov, A.V., 1997, Late Paleozoic–Early Mesozoic Granitoid Magmatism in Altai: Russian Geology and Geophysics, v. 38, p. 755–770.

Webb, L.E. and Johnson, C.L., 2006, Tertiary strike-slip faulting in southeastern Mongolia and implications for Asian tectonics: Earth and Planetary Science Letters, v. 241, p. 323–335.

Wickham, S.M., Alberts, A.D., Zanvilevich, A.N., Litvinovsky, B.A., Bindeman, I.N., and Schauble, E.A., 1996, A stable isotope study of anorogenic magmatism in east central Asia: Journal of Petrology, v. 37, p. 1063–1095, doi: 10.1093/petrology/37.5.1063.

Windley, B.F., Allen, M.B., Zhang, C., Zhao, Z.Y., and Wang, G.R., 1990, Paleozoic accretion and Cenozoic redeformation of the Chinese Tien Shan Range, central Asia: Geology, v. 18, p. 128–131, DOI: 10.1130/0091-7613(1990)018<0128:PAACRO>2.3.CO;2.

Windley, B.F., Kroner, A., Guo, J.H., Qu, G.S., Li, Y.Y., and Zhang, C., 2002, Neoproterozoic to Paleozoic geology of the Altai orogen, NW China: New zircon age data and tectonic evolution: The Journal of Geology, v. 110, no. 6, p. 719–737, doi: 10.1086/342866.

Wing, B.A., Ferry, J.M., and Harrison, T.M., 2003, Prograde destruction and formation of monazite and allanite during contact and regional metamorphism of pelites: Petrology and geochronology: Contributions to Mineralogy and Petrology, v. 145, p. 228–250.

Xiao, W., Windley, B.F., Badarch, G., Sun, S., Li, J., Qin, K., and Wang, Z., 2004, Palaeozoic accretionary and convergent tectonics of the southern Altaids; implications for the growth of Central Asia: Journal of the Geological Society (London), v. 161, no. 3, p. 339–342.

Xinjiang BGMR, 1978, Geologic Map of the Fuyun Area: Unpublished, scale 1:200,000, 1 sheet.

Xinjiang BGMR, 1993, Geologic Map of the Daqiao Area: Unpublished, scale 1:200,000, 1 sheet.

Yang, X., Xie, G., and Li, Z., 1992, Mylonite-migmatite lithogenic series–An important tectono-dynamic rock forming process: Geotectonica et Metallogenia, v. 16, p. 151–159.

Yin, A., and Harrison, T.M., 2000, Geologic Evolution of the Himalayan-Tibetan orogen: Journal of Annual Review of Earth and Planetary Sciences, v. 28, p. 211–280.

Yin, A. and Nie, S., 1996, A Phanerozoic palinspastic reconstruction of China and its neighboring regions, *in* Yin, A. and Harrison, T.M., eds., The Tectonic Evolution of China: Cambridge, Cambridge University Press, p. 442–485.

Zhang, Z., Yan, S., Chen, B., Zhou, G., He, Y., Chai, F., and He, L., 2005, Middle Devonian Picrites of the southern margin of Altay Orogenic belt and implications for the tectonic setting and petrogenesis: Journal of China University of Geosciences, v. 16, p. 95–103.

Zonenshain, L.P., Kuzmin, M.I., and Natapov, L.M., 1990, Geology of the USSR: A Plate-Tectonic Synthesis: Washington D.C., American Geophysical Union, 242 p.

Manuscript Received 22 May 2006
Revised Manuscript Received 22 February 2007
Manuscript Accepted 24 February 2007

Printed in the USA